Geophysical Journal International

Geophys. J. Int. (2019) **217,** 988–1010
Advance Access publication 2019 February 06
GJI Marine geosciences and applied geophysics

doi: 10.1093/gji/ggz074

Constraints on crustal structure of adjacent OCCs and segment boundaries at 13°N on the Mid-Atlantic Ridge

C. Peirce,[1] G. Reveley,[1] A.H. Robinson,[1] M.J. Funnell,[1] R.C. Searle,[1] N.M. Simão,[1] C.J. MacLeod[2] and T.J. Reston[3]

[1]*Department of Earth Sciences, Durham University, South Road, Durham, DH13LE, UK. E-mail: christine.peirce@durham.ac.uk*
[2]*School of Earth and Ocean Sciences, Cardiff University, Park Place, Cardiff, CF103AT, UK*
[3]*School of Geography, Earth and Environmental Sciences, University of Birmingham, Edgbaston, Birmingham, B152TT, UK*

Accepted 2019 February 5. Received 2019 January 30; in original form 2018 July 23

SUMMARY

The 13°N segment of the Mid-Atlantic Ridge is an example of a morphologically well-studied slow spreading ridge segment populated with oceanic core complexes (OCCs). In this paper we present the results of an ∼200-km-long 2-D seismic and gravity transect through this segment, the bounding fracture zones to the south and the ridge discontinuity to the north. We use this transect to consider the two end-member models of OCC evolution in which one, referred to as the *Segment-scale* model, implies they are interconnected with their detachments being part of a single segment-long feature, and the other, the *Localized* model, that each OCC is structurally isolated.

We show, using the 7.5 km s^{-1} velocity contour as the base of crust marker, that the crust is consistently relatively thin ridge-parallel, at ∼5 km thick on average, and that, beneath the OCCs, the Moho marks the top of a velocity gradient transition into the mantle, rather than a distinct velocity discontinuity. Although each OCC is not traversed in an identical structural location, they show a different crustal velocity–density structure with depth, with along axis variations in this structure mirrored by the bathymetric deeps between them. Older OCCs have a contrasting velocity–depth signature to the currently active 13°20′N OCC. The 13°20′N OCC is distinct in that it does not show higher relative velocity at shallower crustal depth like its neighbours, while the 13°30′N OCC has an apparently thinner crust. Our combined *P*-wave seismic traveltime tomography and gravity forward modelling suggests that the OCCs of the 13°N segment are not interconnected at depth. To the north of the 13°30′N OCC, our modelling also suggests that the crust is being magmatically refreshed, or that the ridge axis is currently undergoing magmatic accretion with an associated ridge tip propagation occurring across the ridge discontinuity that marks its northern edge.

The profile also crosses the Marathon and Mercurius fracture zones that mark the southern limit of the 13°N segment and the southern ridge-transform intersection outside corner. Along profile, Marathon fracture zone offsets younger (∼1 Myr versus ∼8 Myr) oceanic crust than Mercurius fracture zone (∼8 Myr versus ∼11 Myr). When considered in combination, both seismic and gravity modelling suggest crustal thinning in the direct vicinity of the bathymetric valley of Marathon fracture zone, coupled with a region of low density that, most likely, reflects serpentinization of the uppermost mantle. In addition, the crust captured between fracture zones appears relatively rotated about an E–W axis and uplifted to the north, with the upwards motion accommodated on the northern lateral edge of the bathymetric depression rather than in its centre. Both the outside corner and the crust bounded by fracture zones have velocity–depth characteristics similar to that of the 13°N segment OCCs rather than normally accreted oceanic crust, particularly in the upper-to-middle crust.

Overall, our results support the *Localized* model of OCC evolution and suggest that fracture zones do not become locked immediately on transform-to-fracture transition as current models dictate.

Key words: Controlled-source seismology; Crustal imaging; Crustal structure; Mid-ocean ridge processes.

1 INTRODUCTION

Mid-ocean ridges characterize the Earth's oceans and are associated with a shallow seafloor, high heat and fluid flow and seismicity; and mark the locations where new oceanic lithosphere is created. Transform faults offset the ridge axes, and fracture zones trace their relict past to the continental margins. As more surveys are undertaken, it is becoming increasingly clear that the mid-ocean ridge setting accommodates a diversity of processes operating over a broad range of inter-related scales and time frames, with crustal formation not being a solely magmatically driven process as was once thought.

1.1 Oceanic core complexes

Since the discovery of domal corrugated surfaces at slow-spreading mid-ocean ridges (Cann *et al.* 1997), our understanding of how seafloor spreading works has undergone major conceptual step-changes in response to the ever-increasing number of high-resolution seabed morphological studies. These domal surfaces, or oceanic core complexes (OCCs) as they have become known, are hypothesized to represent the unroofed plutonic and partially serpentinized mantle footwalls of large-offset normal detachment faults, that appear to accommodate much of the plate separation. These detachment faults are thought to cross-cut the entire crust, exhuming in their footwalls a crustal section typically in the form of a non-corrugated blocky massif, and then, in the domal OCC, mantle rocks intruded by plutonic gabbros (e.g. Tucholke & Lin 1994; Cann *et al.* 1997; Tucholke *et al.* 1998; MacLeod *et al.* 2009; Sauter *et al.* 2013). The domed detachment surface is commonly striated, corrugated in the spreading direction, interpreted as a slip surface that is exhuming a section of the lower crust from beneath the median valley, bounded by blocky topography with widely spaced and back-tilted fault blocks (Smith *et al.* 2006), and accommodates asymmetric oceanic crustal creation (Escartin *et al.* 2008).

Lithological studies of OCCs show that they expose a diverse assemblage of eruptive, plutonic and mantle-derived ultramafic rocks that are highly altered and deformed (MacLeod *et al.* 2002; Escartin *et al.* 2003, 2017; Dick *et al.* 2008), suggesting not only a complex pattern of deformation, but also that significant fluid circulation is focused along the detachment. The link between deformation and hydrothermal activity is supported at the Mid-Atlantic Ridge (MAR) by patterns of local seismicity and the locations of observed hydrothermal venting (Escartin *et al.* 2008), with hydrothermal deposits also observed on OCCs regarded as extinct and preserved in off-axis settings (Escartin *et al.* 2017).

Although it is likely that the corrugated upper surfaces of OCCs represent the exposure of steeply dipping detachments that root at depth beneath the median valley, the link has not been proven, although it is supported to some extent by palaeomagnetic studies that show significant footwall rotation (e.g. Morris *et al.* 2009; MacLeod *et al.* 2011), seismic imaging (e.g. Ranero & Reston 1999, Reston & Ranero 2011; Canales *et al.* 2004) and locations and focal mechanisms of microseismicity (e.g. Parnell-Turner *et al.* 2017). The primary evidence to date is based on *P*-wave traveltime tomographic inversion of two 2-D wide-angle seismic profiles, and passive microseismicity monitoring near the TAG hydrothermal field (deMartin *et al.* 2007; Zhao *et al.* 2012). Here, a steeply dipping band of hypocentres is inferred to mark a fault that flattens abruptly upwards, but does not directly image the detachment rollover, prove the continuity between steep and shallow zones or show the lateral extent of the detachment.

Reston & Ranero (2011) noted that the Atlantis Massif detachment disappeared northwards (towards the segment middle) beneath fault blocks rafted out of the median valley, and suggested that many oceanic detachments did the same, so that OCCs represent locations where a detachment breaks the surface, being covered in the intervening regions by thin-skinned rider blocks of volcanic seafloor. They proposed that the transition from OCC to subseafloor detachment, buried beneath these rider blocks, resulted from increased volcanic infill and less hydration-weakening of the slip surface moving away from the segment end, a hypothesis supported by numerical simulations (Choi & Buck 2012), and noted that the detachment might either extend for the whole segment or die out laterally as magmatic centres were approached. Oceanic detachment faults can, therefore, be regarded as essentially continuous, long-lasting features, linked in the subsurface, active on a segment scale and controlling at least 50 per cent of the total divergence.

Since the early 1990s there has been debate over whether segmentation is controlled top-down by faulting or bottom-up by mantle upwelling (Mutter & Karson 1992; Tucholke & Lin 1994; Tucholke *et al.* 1997). Consequently, if segment-scale detachments control spreading and mantle upwelling within whole segments (e.g. Smith *et al.* 2008; Reston & Ranero 2011; Tani *et al.* 2015; Reston 2018) they could influence patterns of ridge segmentation, and be exceptionally long-lived (Cann & Smith 2005; Escartin *et al.* 2008; Smith *et al.* 2008; Schouten *et al.* 2010; Reston & Ranero 2011).

In an alternative view, MacLeod *et al.* (2009) see OCCs as spatially restricted, structurally isolated, ephemeral features that are switched on and off by variations in local magma delivery and where slip continues as a result of the progressive waning of magma supply to below half that needed to generate a continuous igneous crustal layer to accommodate on-going spreading. In this model, plate separation becomes progressively more asymmetric and the detachment migrates towards and across the axial valley, such that renewed magmatism is intruded into the detachment footwall and ultimately overwhelms it. Spreading becomes strongly asymmetric between such a localized OCC and its conjugate, but not along a whole spreading segment, with spatially restricted transfer zones accommodating the along-strike variation in strain distribution.

Spreading rate asymmetry has been documented at all OCCs studied to date (e.g. Searle *et al.* 2003; Okino *et al.* 2004; Baines *et al.* 2008; Dick *et al.* 2008; Grimes *et al.* 2008) so is clearly an inherent process in detachment fault development. If detachments continue along the entire segment length, they are likely to dominate spreading processes to the extent of controlling the locus of mantle upwelling and the position of the spreading axis (e.g. Mitchell *et al.* 1998), with faulting controlling segmentation (Mutter & Karson 1992) rather than the other way around (Tucholke & Lin 1994; Tucholke *et al.* 1997). In this case, the detachment could be long-lived, with spreading becoming highly asymmetric (Reston 2018). In contrast, if detachments are spatially limited and ephemeral, spreading asymmetry may similarly be restricted to the life span of the detachment.

If a detachment controls mantle upwelling, it is also likely to influence the generation of melt beneath the ridge and to continually capture it to form the lower gabbroic portion of newly accreted magmatic crust in its footwall. These gabbros will be exhumed within the footwall and should form an integral part of the OCC (Ildefonse *et al.* 2007; Olive *et al.* 2010; Schouten *et al.* 2010). In contrast, if melt is only captured and emplaced into the footwall once the detachment root had migrated across the median valley, little gabbro would be expected beneath developing OCCs. Seismic velocity anomalies at the off-axis OCCs of the inactive Atlantis Massif, Dante's Domes and Kane Megamullion have been interpreted in terms of the distribution of gabbros and partially serpentinized peridotites in the detachment footwall and termination (Canales *et al.* 2008), which supports the latter model in which magmatism plays a role in the abandonment of the detachment.

These two models, first postulated by Smith et al. (2006, 2008) and which may actually be end-members, have profoundly different implications for the mode of formation of oceanic lithosphere: one (here termed the *Segment-scale* model) implies a single, laterally extensive long-lived detachment fault that results in most of the lithosphere within an OCC-hosting segment being formed by detachment spreading and uplift of mafic and ultramafic rocks; and the other (here termed the *Localized* model) implies that lithospheric formation driven by extension along detachments, is restricted to the locations of each OCC, with each being structurally isolated. Both models can explain the observed seafloor morphology, however they make different predictions about the distribution of gabbros within actively evolving OCCs, and this may make them distinguishable based on seismic velocity and density.

To understand how oceanic detachment faults and OCCs initiate and evolve and, thus, distinguish between these two models, whole crustal imaging is required. To date, the detachment systems at Atlantis Massif and south of the Kane transform fault along the MAR are amongst the best studied, having been surveyed and sampled using deep-sea vehicles (Blackman *et al.* 2001; Karson *et al.* 2006; Dick *et al.* 2008; Tucholke *et al.* 2013), drilled in the case of Atlantis Massif (Blackman et al., 2006, 2011; Ildefonse *et al.* 2007; Blackman & Collins 2010; Frueh-Green *et al.* 2016), and seismically imaged to a range of crustal depths and resolutions (Canales *et al.* 2004, 2008; Xu *et al.* 2009; Blackman & Collins 2010; Canales 2010; Henig *et al.* 2012; Harding *et al.* 2016). In the Kane area the multiple detachments are considered to be fossilized, and at Atlantis Massif the detachment is considered to be inactive, with microseismicity suggesting that an active rift valley bounding fault is currently dissecting its corrugated surface (Collins *et al.* 2012).

At the ultra-slow spreading (<7 mm yr^{-1}) Mid-Cayman Spreading Centre (MCSC) both the currently active Mt Dent OCC and relic OCCs off-axis have been recently studied by active-source wide-angle seismic imaging (Harding *et al.* 2017; van Avendonk *et al.* 2017; Grevemeyer *et al.* 2018a). These studies show that the currently active hydrothermal systems are underlain by higher velocities in the shallower parts of the crust and that its formation is dominated by periods of magma-poor and magma-rich accretion asymmetrically building a generally quite thin (2–4 km) crust. Despite their distinct difference in spreading rate, the OCCs of the MAR and MCSC have similar morphologies and seafloor lithologies as a comparison between the studies of Escartin *et al.* (2017; and references therein) and Hayman *et al.* (2011 and references therein) demonstrate.

1.2 Transform faults and fracture zones

The relationship between the ridge axis and the transform fault-fracture zone intersection at segment ends, and our understanding of transform faults and fracture zones themselves is less well understood, primarily due to fewer observations which comprise mostly low resolution 1-D or 2-D wide-angle seismic profiles such as, in the Atlantic: Whitmarsh & Calvert (1986) at Charlie-Gibbs fracture zone (FZ); Detrick & Purdy (1980) and Cormier *et al.* (1984) at the Kane FZ; Ludwig & Rabinowitz (1980) and Detrick *et al.* (1982) at Vema FZ; Minshull et al. (1991, 1995) at Blake FZ; and Fox *et al.* (1976) and Sinha & Louden (1983) at Oceanographer FZ, with the crustal structure of north Atlantic fracture zones reviewed by White *et al.* (1984) and Detrick *et al.* (1993). At the East Pacific Rise examples include: the Quebrada, Discovery and Gofar transform faults (Roland *et al.* 2012); and Clipperton FZ (van Avendonk et al., 1998, 2001); and the SW Indian Ridge, the Atlantis II FZ (Müller *et al.* 2000). In contrast, seabed morphology and sampling studies are more common (e.g. Pockalny *et al.* 1988; Tucholke & Schouten 1988).

Transform faults that offset ridge segments are characterized by valleys tens of kilometres wide, whose depth increases as a function of offset distance between the adjacent ridge segment ends. White *et al.* (1984) consider the transform valley to reflect the isostatic response of a thin underlying crust, while Collette (1974) and Pockalny *et al.* (1996) also consider the role of down-faulting due to the thermal contrast between older and younger lithosphere on their opposite sides as part of on-going plate spreading. A transverse ridge is often captured on one side of the transform valley as observed, for example, at the Vema FZ. There the large ridge exposes significant quantities of serpentinized peridotite suggesting not only that they represent a significant fluid flow path to the deeper crust and upper mantle, but also that density driven buoyancy contributes to their elevation (Bonatti, 1976, 1978). Since normal seafloor fabric continues across these fracture zone ridges, Pockalny *et al.* (1996) suggest that they represent the flexural result of trans-tensional extension.

While the shallow bathymetry of the inside corners of ridge-transform-fracture zone intersections is thought to be dynamically supported, and a consequence of opposing plate decoupling across the transform (e.g. Searle & Laughton 1977; Severinghaus & Macdonald 1988; Blackman & Forsyth 1991), the lithosphere of the outside corner is thought to be locked to that across the fracture zone, with lithospheres of different ages strongly coupled (e.g. Tuzo Wilson 1965). Although not common, OCC-like massif features have been observed in the inside corner high position (Reston *et al.* 2002), with similar features mirrored in the outside corner. These massifs are thought to originate by dissection of the inside corner massif by rifting associated with a ridge axis jump, since they both share matching patterns of corrugations on their surfaces and are very similar in dimensions and morphological characteristics. The dissection may be the result of propagation of the spreading axis immediately adjacent, or a new spreading axis forming as a result of readjustment of a non-transform ridge axis discontinuity into either a transform offset or an overlapping spreading centre (Reston *et al.* 2002).

1.3 This study

A number of seismic studies have been undertaken at the MAR, including the ridge segments between 33°N and 35°N (Canales *et al.* 2000; Hooft *et al.* 2000; Hosford *et al.* 2001; Hussenoeder *et al.*

2002), 21°N and 23°N (Dannowski et al., 2010, 2018), the Lucky Strike segment (Singh *et al.* 2006; Seher *et al.* 2010a,b,c; Combier *et al.* 2015) and the Rainbow segment (Canales *et al.* 2017; Dunn *et al.* 2017). To investigate the subsurface structure of OCCs and test the *Segment-scale* versus *Localized* models of OCC along-axis continuity, three research cruises to the 13°N area of the MAR were undertaken, all on the RRS James Cook. Cruises JC102 (Peirce 2014a) and JC109 (Peirce 2014b) undertook a local microseismicity passive ocean-bottom seismograph (OBS) deployment and recovery. The results of this passive imaging have been reported by Parnell-Turner *et al.* (2017). Cruise JC132 (Reston & Peirce 2016) undertook active-source seismic (wide-angle refraction and multichannel reflection), and shipboard gravity, magnetic and swath bathymetry imaging, together with autonomous underwater vehicle (AUV) near-seabed swath bathymetry and magnetic surveying. The combined shipboard and near-seabed magnetics were reported by Searle *et al.* (2016), and their detail analysis is discussed in Searle *et al.* (2018).

Here we describe the results of modelling seismic and gravity data along an ∼200-km-long 2-D transect (henceforth referred to as Profile R—Fig. 1) traversing, south-to-north, both the Mercurius and Marathon FZs, the southern outside corner of the 13°N segment, the Ashadze Complex, OCCs located at 13°20′N and 13°30′N on the western ridge flank, the ridge axis deviation in trend centred at 13°35′N, and the youngest oceanic crust of the eastern ridge flank to the north. This 2-D profile also traversed through the 3-D tomographic seismic grid acquired over the 13°20′N and 13°30′N OCCs (henceforth referred to as 1320 and 1330, Fig. 1) during the same cruise, to specifically determine their internal structure and the geometry of the detachment surface. The results of the 3-D tomography-based modelling have been reported by Simão *et al.* (2016), and will be published elsewhere (forthcoming Simão *et al.* 2019).

2 GEOLOGICAL SETTING

An extensive region of OCCs exists at 13°N on the MAR and includes two located at 13°20′N and 13°30′N (Fig. 1) that are thought to be in the active and dying stages of evolution and development, respectively; two further OCCs, together called the Ashadze Complex (centred at 13°05′N), are considered to be relict (e.g. Cherkashov *et al.* 2008). A number of OCCs are also fossilized in the bathymetry off-axis and a prominent inside corner high exists at the southern ridge-transform intersection, being the shallowest, but spatially restricted, seabed within the 13°N region.

The OCCs of the 13°N segment have been surveyed with shipboard multibeam bathymetry, gravity and magnetic surveying (e.g. Smith et al., 2006, 2008; Mallows & Searle 2012), imaged with TOBI near-bottom side-scan sonar, sampled with dredges and a seabed rock-drill (e.g. Searle *et al.* 2007a,b; MacLeod *et al.* 2009), surveyed and sampled using an ROV to map seabed morphology and lithology (e.g. Escartin *et al.* 2017), and show the characteristic features expected of an OCC (Escartin & Canales 2011) which, heading from off-axis to on-axis, are:

(1) an outward-tilted breakaway ridge;
(2) a blocky massif comprising a crustal section;
(3) a domal and striated massif of mantle and plutonic rocks and
(4) a bounding hanging wall cut-off towards the MAR axis.

Both the *Segment-scale* and *Localized* detachment hypotheses are based on observations from this area (e.g. Smith *et al.* 2008; MacLeod *et al.* 2009; Schouten *et al.* 2010; Escartin *et al.* 2017).

The 1320 and 1330 OCCs are located on the western flank of the MAR axial rift valley and were first identified by Smith *et al.* (2006) from shipboard geophysical surveys, in a section of the ridge axis that is characterized by reduced melt supply. These OCCs are ∼7 km and ∼12 km wide along axis, respectively, and are ∼5.5 and ∼8 km long in the spreading direction demonstrating that extension, at a half-rate of 12 km Myr^{-1}, may have been on-going along each detachment for ∼0.5 and ∼0.7 Myr, assuming symmetrical spreading. Tectonic interpretation of near-bottom sonar imagery suggests that the 1320 detachment may still be active, whereas the 1330 detachment may be dying or inactive, given the observed propagation of adjacent volcanic ridges to the north, volcanic craters surrounding the 1330 OCC and an apparent termination of the detachment fault (MacLeod *et al.* 2009; Mallows & Searle 2012).

Dredging, seafloor sampling with ROVs, and subseafloor rock drilling at these detachment faults has yielded a wide range of lithologies consistent with the exposure of normally deep-seated rocks (gabbro and peridotite) in addition to basalts, and deformed fault rocks and mass-wasted rubble (MacLeod *et al.* 2009; Pertsev *et al.* 2009; Escartin *et al.* 2017). Geochemical analysis of the recovered basalts reveals a change in magmatic activity from a magma-poor phase at the initiation of detachment faulting, to a more magma-rich phase at the present time (Wilson *et al.* 2013).

Several active and extinct hydrothermal fields have been found within the 13°N segment (Fig. 1), including on the exposed 1320 and 1330 detachment surfaces (Fig. 2,Beltenev *et al.* 2007; Cherkashov *et al*. 2010b, 2013, 2016; Pertsev *et al.* 2012; Bortnikov *et al.* 2015). The 1330 vents have been dated at up to ∼100 kyr in age and show no apparent age progression with location in the direction of spreading, with older deposits found near the axis and active sites more than 5 km off-axis (Cherkashov *et al.* 2010a).

The 13°N segment is bounded to the south by a double transform-fracture zone system (Marathon and Mercurius FZs—separated by ∼50 km in an along-axis direction) and to the north by the Fifteen-Twenty FZ. The 1330 OCC lies in the equivalent location of an inside corner, with respect to a deviation in trend in ridge axis morphology. Together these features make this region the ideal target for studying not only ridge segment evolution, but also the crustal structure and setting of OCCs.

3 DATA ACQUISITION AND PROCESSING

Profile R was acquired during RRS James Cook research cruise JC132 (Reston & Peirce 2016) which took place in January and February 2016, with port calls in Mindelo (Cape Verde) and Port of Spain (Trinidad and Tobago) where, in the latter case, an absolute gravity base station was also re-established.

3.1 Swath bathymetry data

A hull-mounted Simrad EM120 multibeam echo sounder acquired depth soundings throughout JC132. The water column sound velocity was also measured, centrally within the study area to a depth of ∼4 km, to calibrate the swath system and inform ray trace modelling of water waves for OBS relocation purposes, and inclusion of the water column in each seismic model.

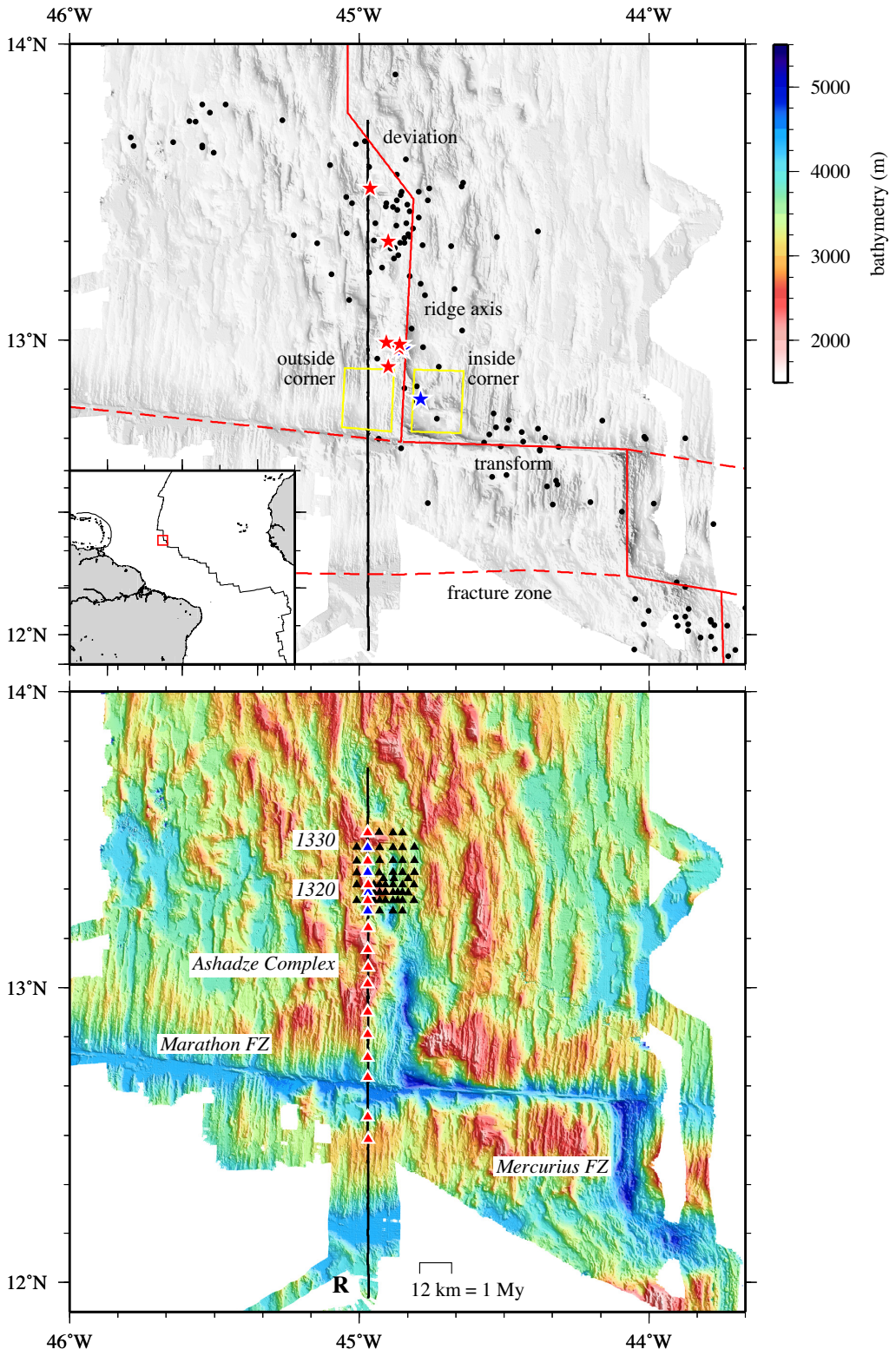

Figure 1. Bathymetry of the 13°N region of the Mid-Atlantic Ridge (lower panel), showing the location of Profile R (solid black line) and the OBSs modelled in this study (white outlined triangles), together with its intersection with a 3-D grid of OBSs (black triangles) also deployed during JC132 (Simão *et al.* 2016 and forthcoming Simão *et al.* 2019). OBSs (marked by blue filled triangles) only recorded shots fired along a co-incident profile acquired as part of the 3-D grid and were recovered prior to shooting Profile R. The locations of the 1320, 1330 and Ashadze Complex OCCs are labelled together with the Marathon and Mercurius fracture zones. The upper panel shows the current ridge-transform geometry and nomenclature adopted, together with the location of teleseismic earthquakes (black dots) and hydrothermal vents (red stars—active vents; blue stars—inactive). See text for details. Inset (left) shows the location of the work area (red box).

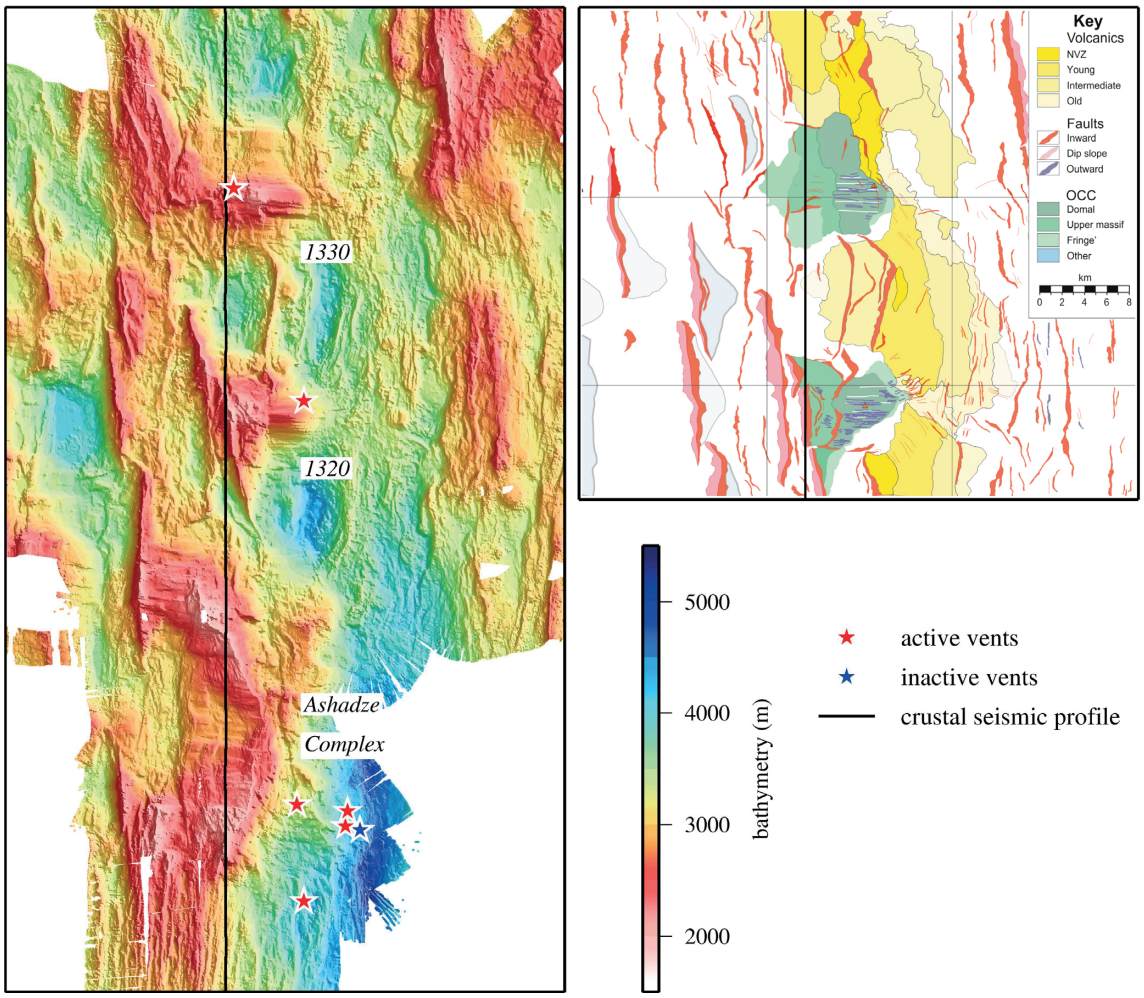

Figure 2. Bathymetry of the oceanic core complexes of the 13°N region of the Mid-Atlantic Ridge. Left-hand panel shows the location of Profile R and its crossing point for each labelled OCC, together with the location of active (red stars) and inactive (blue stars) hydrothermal vents. The swath bathymetry data shown has a 4 m lateral resolution. Upper right-hand panel shows a morphological and structural interpretation of seabed features for the 1320 and 1330 OCCs plotted at the same scale as the bathymetry (after Mallows & Searle 2012), indicating that Profile R crosses these OCCs in the vicinity of the breakaway-upper massif.

The swath bathymetry data set was cleaned to remove bad soundings, merged with swath data from previous cruises (JC007—Searle *et al.* 2007c; JC102—Peirce 2014a; JC109—Peirce 2014b) and gridded at ∼100 m node spacing for the entire study area (Fig. 1), and at ∼4 m in the vicinity of the OCCs (Fig. 2), the latter made possible by the high density of repeat transects. Fig. 2 shows where Profile R traverses each of the 1320, 1330 and Ashadze Complex OCCs, together with a seabed morphological reference context showing, in particular, the location of the domal surface, upper massif, breakaway and regions of recent volcanism at the seabed surrounding the 1320 and 1330 OCCs (after Mallows & Searle 2012). Given the seismic Fresnel zone width (∼1 km) at their average seabed depth, Profile R traverses the OCCs at, or in the vicinity of, the centre of the exposed detachment fault (Ashadze), the breakaway (1320), and just after breakaway (1330) based on the interpretations of Smith *et al.* (2008) and MacLeod *et al.* (2009). To the north of 1330, Profile R crosses a region of young volcanic features on the seabed and the ridge-axis neovolcanic zone. Fig. 3 shows that, to the south, the profile crosses the apparent volcanic abyssal hill fabric of the outside corner (*cf.* Fig. 1), the >4500-m-deep sediment-filled Marathon FZ that also contains an off-profile ridge-like feature that rises above the current level of sediment infill (Fig. 3d), ∼8 Ma oceanic crust and, finally, the >10 km wide, flat sedimented terrain of the Mercurius FZ (Fig. 3c).

The main tectonic features of the 13°N segment are summarized in Fig. 1, with active and inactive hydrothermal vents (InterRidge Vents Database v3.4—https://vents-data.interridge.org/) and earthquakes of magnitude greater than 3.0 M_b that have occurred since 1980 (United States Geological Survey Earthquake Hazard Program—https://earthquake.usgs.gov/earthquakes/) shown for reference.

3.2 Seismic data source

Contemporaneous acquisition of WA and MCS data was enacted with a 60 s shot interval to prevent water wave wrap-around interfering with first arriving phases recorded by the OBSs, whilst still achieving a reasonable MCS reflection data fold. The seismic source consisted of a 12 Bolt airgun array, with a combined volume of 4300 in^3 (70.5 l), towed 8 m below the sea surface and fired at 2000 psi (142 bar).

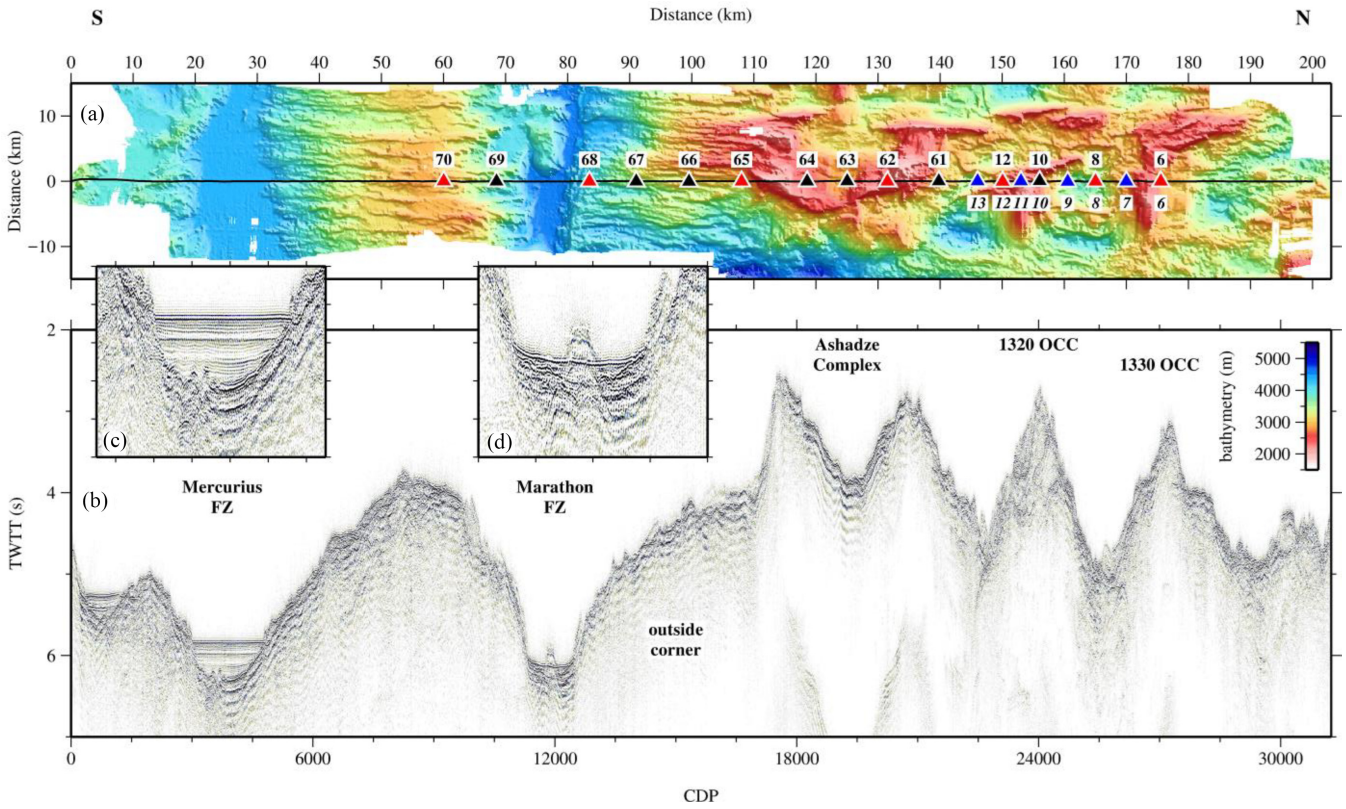

Figure 3. Profile R. (a) Acquisition geometry showing the bathymetry, shots fired (solid black line) and OBSs (triangles) projected into kilometre offset model space. OBSs annotated in italics recorded a co-incident profile from the 3-D grid and have been included in the analysis. The record section data for OBSs marked by red triangles are shown in Figs 4 and 10. (b) Corresponding MCS record section (plotted in two-way traveltime—TWTT) showing the rugged, generally sediment-free terrain of the ∼0–1 Myr age crust accommodating the OCCs (annotated), the curved bathymetry of the outside corner, and the Marathon and Mercurius FZs. The processing scheme is outlined in Section 3.3. (c) Enlargement of the Mercurius FZ showing its generally flat-lying sediment infill. The deeper, older layers show an arcuate up-lap against the northern edge of the fracture zone, suggesting a phase of differential uplift. (d) Enlargement of the Marathon FZ showing its thinner sediment accumulation and matching arcuate reflector pattern which, given its younger age, reaches the seabed and suggests differential motion is on-going. An out-of-plane basement high is also imaged, located to the west of the profile.

3.3 MCS data acquisition and processing

MCS reflection data were recorded solely for the purpose of imaging the thickness of any sediment cover on the older crust south of the Marathon FZ and within the fracture zones themselves, to inform initial seismic model construction required for WA traveltime pick inversion. The MCS data were acquired using a 3 km long, 240-channel streamer with 12.5 m group interval, which was towed at 10 m depth. At the average ship speed of ∼4.5 kn, a shot spacing of ∼150 m yielded a maximum theoretical fold of 10. Given this relatively low fold, traces were resorted into 25 m super-bins, which increased the average fold of cover from 10 to ∼40 and significantly improved the reflectivity of the intrasediment and basement reflectors (Fig. 3b). MCS data processing involved application of pre-stack Kirchhoff time migration and normal moveout correction with a velocity of 1500 m s^{-1} and stacking, followed by post-stack spiking deconvolution to reduce source signature reverberation, since the airgun array was tuned for deep crustal WA acquisition primarily, and was inherently reverberative as a consequence, given the larger chambered airguns that comprised the array. The fully processed data from the MCS profiles within the 13°N WA grid, acquired with a different airgun array design and shot firing rate, will be published separately.

In this study, the MCS section is used solely to locate and measure the thickness of any sediment cover (Fig. 3b) and it shows that little-to-no sediment cover exists along the entire length of Profile R. However, the section does also reveal the contrasting structures of the Mercurius (Fig. 3c) and Marathon (Fig. 3d) FZs, with the former having a thicker sequence of layered accumulated sediment and the latter being intersected closer to the ridge-axis such that sediment has had less time to accumulate. It is appropriate to comment on the observed features in the MCS section at this point, since they are of a scale unresolvable by the WA data and its modelling.

Marathon FZ contains an out-of-plane feature (Fig. 3d) that we attribute to a basement fragment or small transverse ridge, captured within and on the southern side of this fracture zone, immediately to the west of Profile R (Fig. 3a), similar to that observed at the Vema FZ (Lagabrielle *et al.* 1992). Within the Mercurius FZ (Fig. 3c) the intrasediment layering reveals the relative motion between the north and south sides of this FZ, with the arcuate up-lapping nature of the deeper layers on the northern side suggesting a degree of relative uplift of the younger lithosphere, which does not appear to have continued to the present-day. Within the Marathon FZ, similar sediment layering is imaged, with uplift of the younger lithospheric side continuing along the northern side of the valley until much

more recently. The outside corner itself has a curved characteristic, while the older lithosphere captured between the FZs has a shallower topographic gradient to the south than to the north which suggests a more rotational block-like aspect.

3.4 WA seismic data set

WA seismic data were recorded by 14 OBSs deployed between ∼7 and 15 km apart along-profile depending on the seabed topography, with the largest intra-OBS gap being located at the Marathon FZ due to the greater water depth there exceeding the maximum instrument operational depth. In addition, data recorded by four further OBSs (7, 9, 11 and 13–Fig. 3a) deployed along a co-incident profile within the 3-D grid survey (Fig. 1–Simão *et al.* 2016 and forthcoming Simão *et al.* 2019) were also included in the Profile R modelling. Each OBS recorded data at 4 ms (250 Hz) sampling interval from a hydrophone, vertical geophone, and two horizontal geophone components, over 60 s trace lengths. Instrument-seabed coupling and variations in seabed topography control the signal-to-noise ratio (SNR) and the primary traveltime characteristics of seismic phases recorded by each instrument.

Fig. 4 shows two example WA record sections from OBSs 12 and 68. For OBS 12 (Figs 4a and b) located on the southern flank of the 1320 OCC, distinct first arriving phases, identified as crustal *P*-wave refracted arrivals (Pg), are observed to offsets of ∼30 km to the north and south of the instrument location, with the variation in arrival time largely reflecting the variation in seabed topography along profile. There is little equivocal evidence for mantle refracted arrivals (Pn—e.g. OBS 68—Figs 4c and d) or Moho reflections (PmP). This characteristic is shared by all OBSs located south of OBS 12 to the north flank of Marathon FZ, sited on lithosphere less than ∼1 Myr old. Each OBS located on 8 Myr old lithosphere between FZs recorded arrivals out to offsets of ∼60 km for shots fired from the south, while for shots fired to the north of these instruments arrivals were recorded only to offsets of ∼30 km. Similarly, secondary arriving *S*-waves are primarily observed on record sections for OBSs located south of Marathon FZ.

3.5 Potential field data acquisition

Gravity data were acquired port-to-port using a Lacoste & Romberg Micro-G Air-Sea gravimeter. These data were processed, incorporating Eötvös and drift corrections, and tied to absolute stations to calculate the free-air anomaly (FAA, Fig. 5c). For the region to the north of the Marathon FZ, where there are numerous intersecting profiles from all three cruises (JC102–Peirce 2014a; JC109–Peirce 2014b; JC132–Reston & Peirce 2016) that were all acquired with the same gravimeter, crossover analysis gives an average data set uncertainty of ±5–10 mGal depending on location, surveying speed and sea state. Magnetic data were acquired only during JC132 (Reston & Peirce 2016) with a SeaSpy magnetometer, deployed only during seismic surveying. These data were processed to apply a lay-back correction for tow cable length behind vessel and filtered to remove spikes resulting from cable pick-up of ship-generated electrical noise, and the airgun firing electrical pulses. Finally, the International Geomagnetic Reference Field (v12—Thébault *et al.* 2015), calculated for the work area, was subtracted to provide the total field magnetic anomaly (Fig. 5e), which was further reduced to the pole (Fig. 5f) to better reveal the positive and negative magnetization pattern. Here, the magnetic data are used solely to inform seismic model interpretation and their processing and detailed interpretation are published in Searle *et al.* (2018). The gravity data will be used to test the uniqueness of the best-fitting seismic model and will be discussed further in Section 6.

4 2-D MODELLING

4.1 WA seismic data modelling

First arrival traveltimes were picked, wherever possible using unfiltered data, from the hydrophone record for each instrument, as this displayed the highest SNR. Pick phases were assigned based on the offset and apparent velocity of the arrivals. A pick uncertainty of 50 ms, calculated based on instrumentation and shot location errors, was assigned for each subseabed travelling phase regardless of shot-receiver offset and, thus, turning depth. Approximately 7600 first arrival traveltime picks were made.

The *FAST* method of Zelt & Barton (1998) was used for 2-D inversion modelling. The model seabed interface was created by sampling the bathymetry data at 0.25 km intervals along profile, and projecting these and the OBS and shot locations into kilometre-space relative to a model 0,0 located at 11°56.76′N/44°58.2′W. The model was discretized on a 0.25 km by 0.25 km uniform square mesh, which remained constant throughout modelling. Prior to inversion, OBS instrument locations on the seabed along-profile were accurately determined by forward ray trace modelling, using *rayinvr* (Zelt & Ellis 1988; Zelt & Smith 1992), of the water wave arrivals (Pw) using a water column velocity structure defined by sound velocity profiles.

Since no sediment cover of any significant thickness was observed along profile, the initial inversion model had a simple 1-D velocity–depth profile applied beneath the seabed (Fig. 6a), increasing from 2.5 km s^{-1} at the seabed to 7.5 km s^{-1} at ∼5 km subseabed. Below this, the velocity was increased to 8.5 km s^{-1} at ∼10 km subsea surface to represent a constant-depth Moho, although no first-order velocity discontinuity was imposed. This starting model was chosen to enable the greatest degree of modelling freedom without unduly biasing the inversion outcome by applying any preconceived idea of crustal structure.

Modelling comprised one run of five non-linear inversion iterations followed by one run of three iterations, with the inversion cell size reduced between runs, and the model outcome of the first run used as the starting model for the second. During the first run, 1.0 km by 1.0 km inversion cells were used to develop the larger-scale velocity structure of the model (Fig. 6b). For the second run, 0.5 km by 0.5 km inversion cells particularly refined the velocity structure beneath the OCCs (Fig. 6c), resulting in a final root mean square traveltime misfit of 135 ms, equivalent to a χ^2 of ∼5.3, and an improvement from a χ^2 of ∼21.4 of the first run (Fig. 6b).

On initial inspection, the final inversion velocity model (Fig. 6c) displays a velocity structure with features that mirror the seabed topography of the OCCs, with higher velocity at shallow crustal level beneath the Ashadze Complex and 1330 OCC, but not beneath the 1320 OCC. Similarly, crustal thinning is observed to the north and south edges of the Ashadze Complex, and beneath the 1330 OCC itself, while the outside corner reveals a relatively thicker crust than elsewhere along profile.

As often noted in inversions, acquisition geometry-related smearing is observed but is limited primarily to a region beneath the southern flank of the Ashadze Complex. An apparent velocity inversion

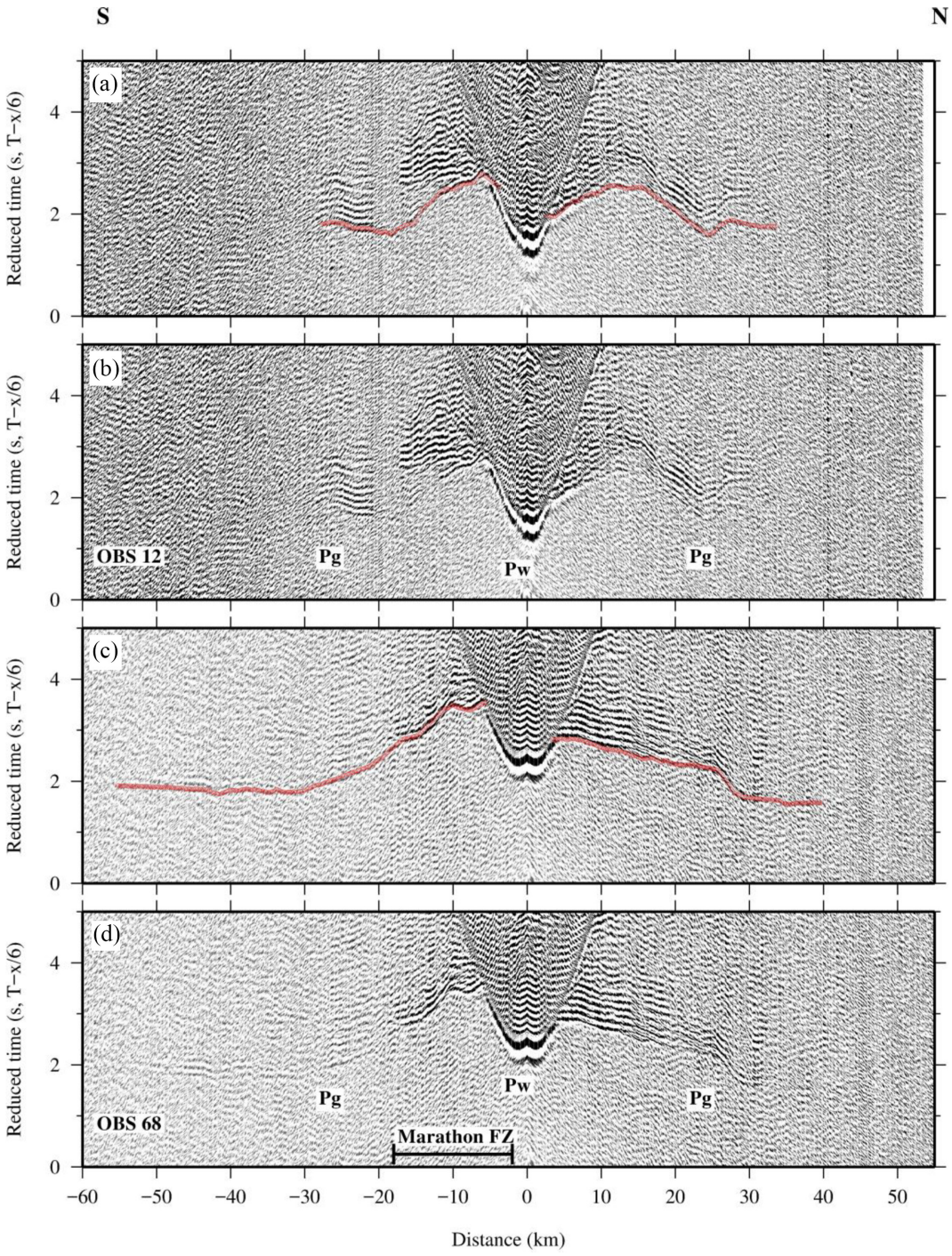

Figure 4. Example hydrophone record sections for OBSs 12 (a and b) and 68 (c and d). See Fig. 3(a) for location. Record sections show filtered hydrophone data plotted at a reduction velocity of 6 km s^{-1}. Traveltime picks have been plotted as red dots of diameter equivalent to the pick uncertainty. Crust (Pg) and water wave (Pw) phase identifications are annotated. The location of Marathon FZ in relation to OBS 68 is also indicated, corresponding to a significant decrease in signal amplitude.

in the lower crust beneath the 1320 OCC is also interpreted as a modelling artefact. Also noteworthy is the region of mantle-type velocity at shallower depth, relative to the surrounding crust, beneath the southern flank of the Marathon FZ, rather than beneath the fracture zone itself. The features of this model, henceforth called the *inversion model*, and their interpretation will be considered in Section 5.

4.2 Inversion model resolution testing

Checkerboard testing of the *inversion model*, adopting the approach of Zelt (1998), was used to determine the smallest structures and velocity variations resolvable by the acquisition geometry and model parametrization (Fig. 7). A velocity perturbation checkerboard pattern was added to the *inversion model* and then synthetic traveltimes

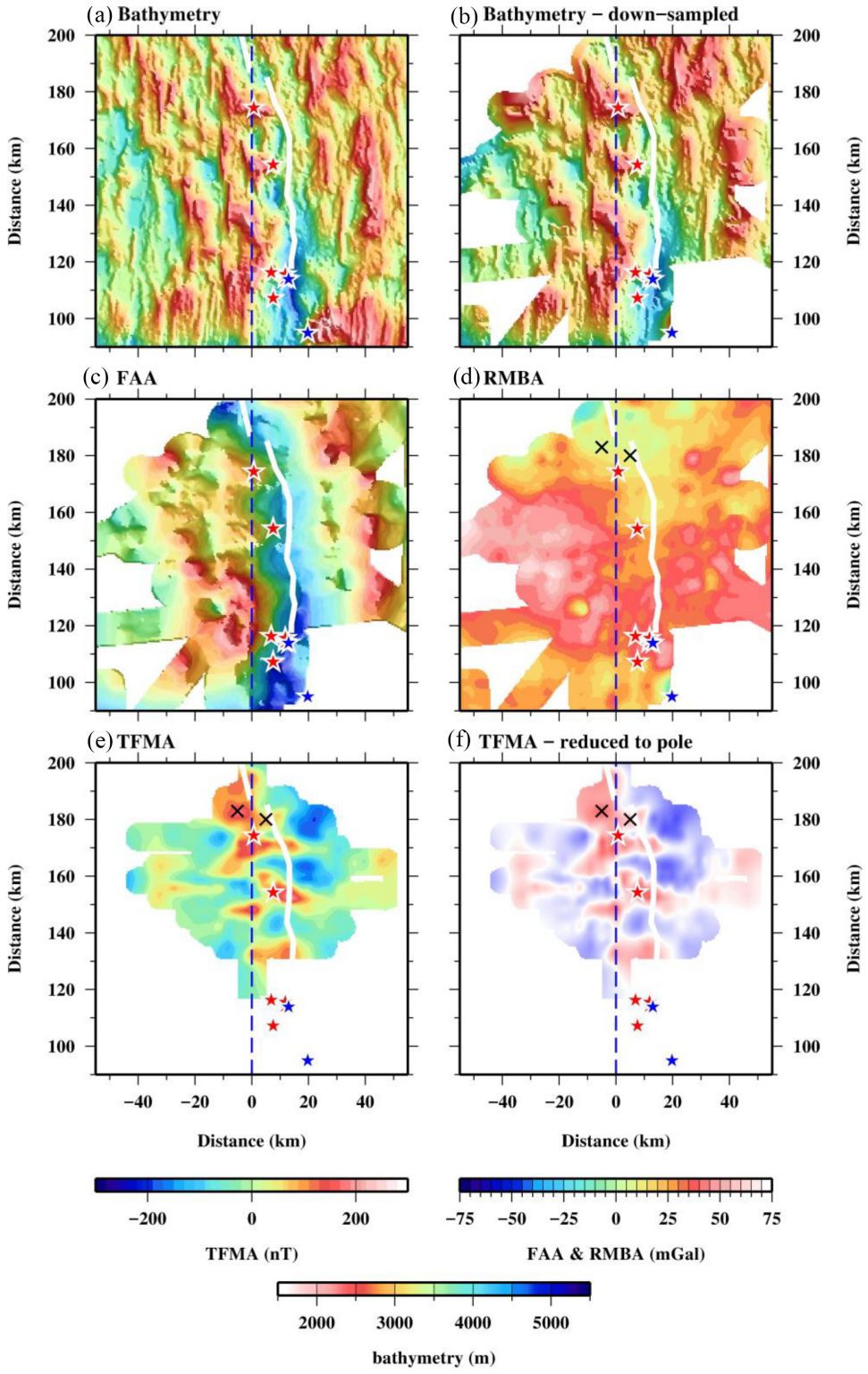

Figure 5. Comparison of potential field anomalies with bathymetry. (a) Swath bathymetry. (b) Bathymetry, down-sampled to match the lateral resolution of the FAA, used in the calculation of the RMBA. (c) Free-air anomaly (FAA). (d) Residual mantle Bouguer anomaly (RMBA). (e) Total field magnetic field anomaly (TFMA). (f) Reduced to the pole magnetic anomaly showing the pattern of positive (red) and negative (blue) magnetization throughout the 13°N axial region. In particular, the ridge-axis does not consistently show the positive magnetization pattern expected for the current chron. The blue dashed line locates Profile R and the stars active (red) and inactive (blue) hydrothermal vents. The thick white line marks Mallows & Searle's (2012) interpreted ridge-axis location. The anomaly pairs discussed in the text are marked by crosses.

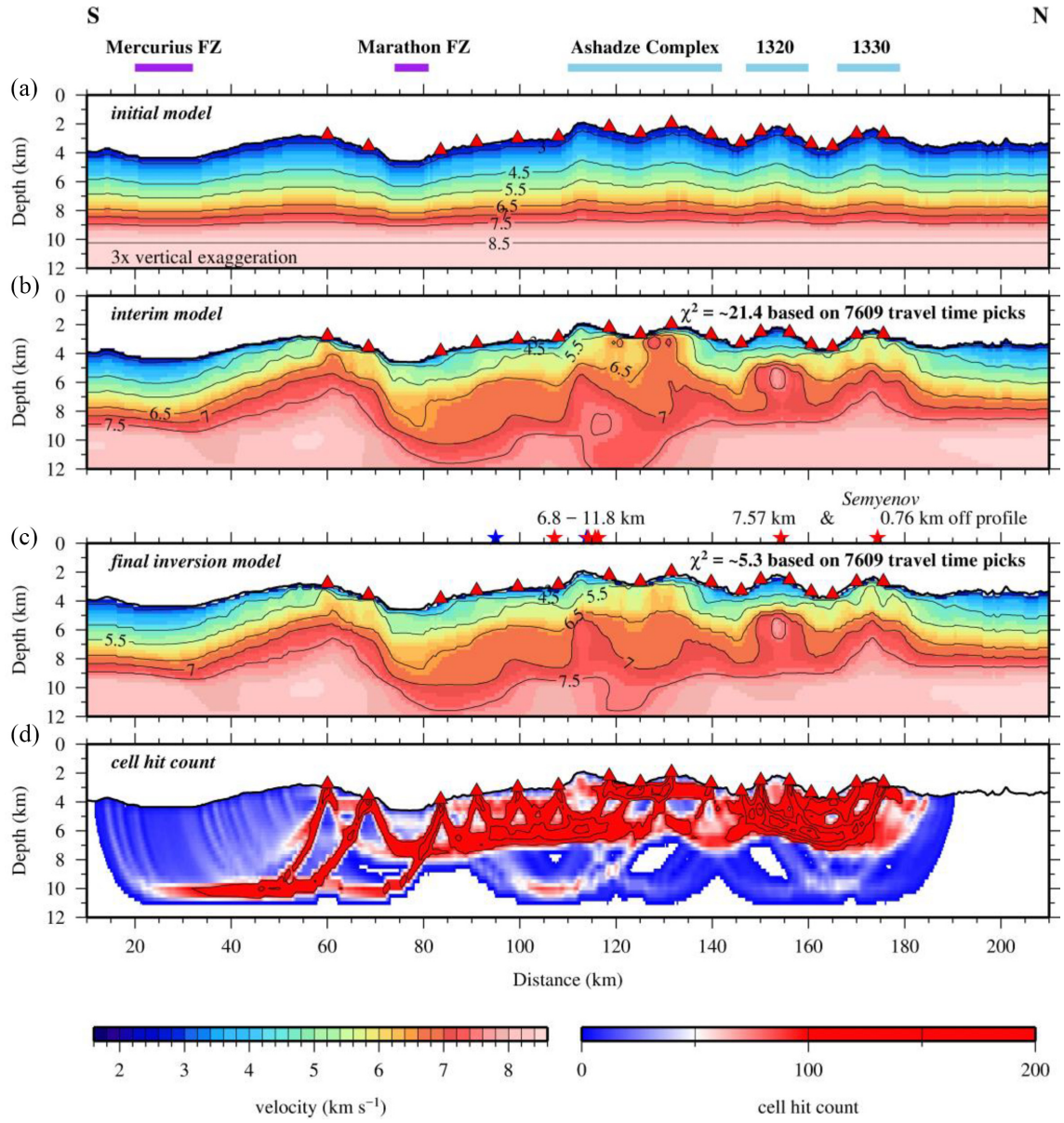

Figure 6. Inversion modelling. (a) Initial model showing the 1-D velocity–depth profile beneath the seabed. OBS locations are marked by red triangles, and prominent topographic features are annotated above. (b) Interim model achieved after the first inversion run within an inverse cell size of 1.0 km x 1.0 km. (c) Final *inversion model* achieved after a further run with a cell size of 0.5 km x 0.5 km. Vent sites are marked by stars above (red—active vents; blue—inactive), with their distance off-profile annotated. The Semyenov field is labelled. (d) Cell hit count indicatively showing the areas of the model well covered with rays traced as part of the inversion process. For parts a–c) model velocities are contoured at 0.5 km s^{-1} intervals.

were calculated using the shot-receiver offsets of the observed traveltime picks. Random Gaussian noise was then added to these synthetic traveltimes corresponding to the pick uncertainties, prior to their inversion using the same parameters as those used to derive the *inversion model* itself.

In addition to investigating the resolution in terms of scale of feature and velocity error bound, we also investigated if the imposed checkerboard pattern in itself affects the resolution outcome, or imposes a form of aliasing. In all tests, a full suite of patterns was tested that included aligned patterns vertically (columns) and horizontally (rows), alternation of the polarity of the checkerboard velocity (positive and negative), half shifts in cells (across rows and down columns) and all possible combinations thereof—16 patterns in total; and all applied to a broad range of cell sizes of different vertical and horizontal sizes, and scales (expressed as per cent) of velocity perturbation. What this testing shows is that there is a significant difference in outcome between imposed patterns, that leads to the conclusion that the pattern chosen has a significant control over the recovery in itself. Here we show the 'at best' outcomes of the test process for the upper crust (Figs 7a–c), to mid-crustal depth (Figs 7d–f), and throughout the crust as a whole along the entire profile (Figs 7g–i), where the outcomes (demonstrated by the semblance, Zelt 1998) are masked by the ray coverage. We adopt Zelt's (1998) semblance threshold of 0.7 to define the parts of the model that are considered to be well resolved. However, semblance can be misleading as it is dependent on the operator radius. We use an operator radius set to the checkerboard cell size, which is larger

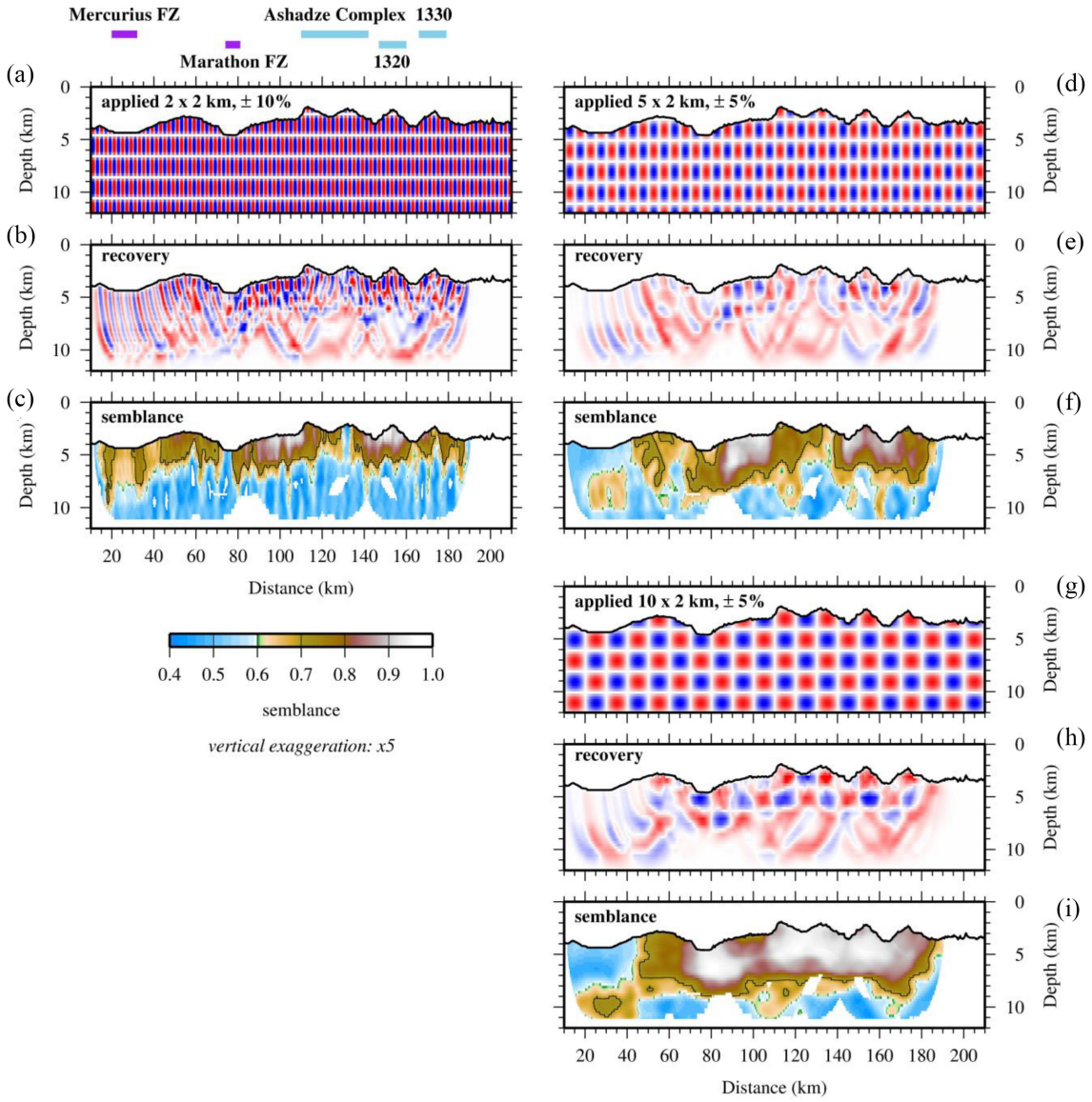

Figure 7. Resolution testing of the *inversion model* (*cf*. Fig. 6c). (a) Applied 2 km x 2 km 10 per cent velocity anomaly checkerboard. Prominent topographic features are annotated above. (b) Checkerboard recovery. (c) Corresponding semblance, showing that the inversion process resolves features of this scale and velocity bound throughout the upper crust along the majority of the profile. (d) Applied 5 km x 2 km 5 per cent velocity anomaly checkerboard. (e) Checkerboard recovery. (f) Corresponding semblance, showing that the inversion process resolves features of this scale to mid-crustal depths for the profile to the north of Mercurius FZ. (g) Applied 10 km x 2 km 5 per cent velocity anomaly checkerboard. (h) Checkerboard recovery. (i) Corresponding semblance, showing that the inversion process resolves features of this scale to base of crust and uppermost mantle depths for the profile to the north of Mercurius FZ. The thin black contour in all semblance panels indicates which parts of the model are well recovered using a semblance of 0.7 as the threshold criteria. All checkerboard recovery and semblance plots are masked showing only areas covered by ray coverage (*cf*. Fig. 6d).

than both the forward cell size (0.25 km x 0.25 km) and inverse cell size (first run—1.0 km x 1.0 km; second run—0.5 km x 0.5 km).

Figs 7(d)–(f) show that, for an applied ±5 per cent velocity anomaly, structures larger than 5 km x 2 km should be resolvable to ∼6-km-depth below sea level (bsl) between 50 and 180 km along-model distance, and particularly well resolved within ∼2–3 km subseabed where the semblance threshold of 0.7 is exceeded (Fig. 7f). Within the upper few kilometres of the crust, structures as small as 2 km x 2 km should be resolvable with a ±10 per cent velocity limitation (Figs 7a–c), where ray coverage (as indicatively represented by the cell hit count–Fig. 6d) is highest, particularly beneath the 1320, 1330 OCCs, Ashadze Complex and the outside corner. Over this crustal depth range, the choice of the applied pattern had a particularly high influence over the outcome, together with there also being a clear trade-off between scale of applied cell size and scale of applied velocity perturbation dictating the resolution achievable. Between Mercurius FZ and 180 km along-model distance, structures larger than 10 km x 2 km with a ±5 per cent velocity anomaly should be resolvable at lower crust and uppermost mantle depths. Ray coverage and the recovery of the imposed checkerboard are consistently poorest below 8 km bsl to the north of 80 km along-model distance, reflecting the apparent absence of longer-offset observed arrivals and, consequently, that marks the depth to which the model may be interpreted with any confidence. Overall, though, the resolution testing indicates that the internal velocity structure of each OCC should be independently

resolvable and, consequently, so should their along-ridge-axis interrelationship.

4.3 Gravity anomaly modelling

The observed free-air gravity anomaly (FAA—Fig. 5c) provides an independent test of velocity model uniqueness and gives additional constraint on poorly resolved regions. However, given that Profile R runs from ∼11.5-Myr-old lithosphere in the south to effectively 0-Myr-old lithosphere north of ∼75 km model distance, crossing two fracture zones, the ridge-axis thermal anomaly was calculated and subtracted from the FAA using the approach outlined in Peirce *et al.* (2001) and Peirce & Navin (2002), following the method of Forsyth (after Phipps Morgan & Forsyth 1988, as developed from Forsyth & Wilson 1984). When applied in addition to the mantle Bouguer anomaly (MBA) approach of Parker (1972), this results in the residual mantle Bouguer anomaly (RMBA, Fig. 5d). To calculate the MBA a constant crustal thickness of 5 km was assumed beneath the swath-defined (down-sampled to match the lateral resolution of the FAA anomaly) seabed (Fig. 5b), with sea water, crust and mantle densities of 1035, 2700 and 3300 kg m^{-3}, respectively.

The *inversion model* was converted into a density model consisting of 2-D polygons with upper and lower boundaries based on the 4.5, 5.5, 6.5 and 7.5 km s^{-1} velocity contours, considered indicative of traditional oceanic crustal layering (White *et al.* 1992), and where model edge effects were prevented by extending the density structure for 1000 km beyond the model limits. As part of testing, the veracity of suspected inversion artefacts was also investigated at this point, particularly those located at 115, 8 km (offset, depth co-ordinates) and 60, 8 km in the model.

As a starting point, the Carlson & Raskin (1984) standard velocity–density relationship for the oceanic crust was applied to construct the initial density–depth model, with a constant density defined for each layer within the crust, a density of 1035 kg m^{-3} assigned to the water column, and 3330 kg m^{-3} for the mantle. The expected free-air gravity anomaly was then calculated (Fig. 8) using *grav2d*, modified from the original programme written by J.H Luetgert based on the algorithm of Talwani *et al.* (1959), and compared to the thermally corrected observed FAA (black line in Fig. 8c).

Although a good fit within the ± 10 mGal error in the FAA was achieved along the majority of the model for this constant density layered model (Fig. 8a—blue line in Figs 8c and d), within the *inversion model* sensitivity limits, suggesting that it is a good overall representation of actual crustal structure; this fit was only achieved by removing the apparent thinning of the crust centred at 115, 8 km and 60, 8 km. Consequently, these features are considered to be artefacts of the inversion process.

However, a mismatch up to ±20 mGal remains associated with Marathon FZ, the Ashadze Complex and, to a lesser extent, the 1320 OCC. Consequently, this density–depth model was divided into a series of lateral zones within which the density could be relatively adjusted, whilst still lying within the velocity error constraints, and modelling progressed to achieve the best fit to the observed anomaly (to within ± 10 mGal error along the entire profile length), in particular for regions poorly constrained by seismic ray coverage. The best-fitting density–depth model (henceforth referred to as the *density model*) is shown in Fig. 8(b) and its fit to the observed FAA shown in Figs 8(c) and (d) (red line). The features of this *density model* will be discussed in Section 5 together with the conclusions drawn from all aspects of the seismic modelling.

4.4 Forward velocity modelling

4.4.1 Inversion artefacts

As a means of further testing the features of the inherently smoothed and interface-free *inversion model* it was converted into a forward node-specified model with distinct layer boundaries incorporated (Fig. 9b), using the 5.5 and 6.5 km s^{-1} velocity contours to define intracrustal interfaces and the 7.5 km s^{-1} velocity contour chosen to represent the base of crust (black line boundaries in Fig. 9b). The observed traveltime picks (Pg and Pn phases) were then point-to-point ray traced using *rayinvr* (Zelt & Ellis 1988; Zelt & Smith 1992—Fig. 9d) to first appraise the validity of phase assignment, particularly given the effect of variation in seabed topography on arrival trend with offset within each record section, and then to further test the model fit and identify likely artefacts (marked by black stars in Fig. 9d) in the *inversion model*. The result of this modelling is shown in Fig. 9(d) (ray diagram) and Fig. 9(e) (traveltime pick fit) and shows a χ^2 of ∼5.5 based on ∼5800 matched picks.

Similarly, the best-fitting *density model* was also tested using the base of its deepest blocks to alternatively define the Moho (white line boundaries in Fig. 9c), except in the vicinity of Marathon FZ. Here, the possibility that the 3100 g cm^{-3} block represents serpentinized uppermost mantle was also tested, by using the top of this block to represent the Moho. The result of point-to-point ray tracing the same traveltimes through the resulting model (Fig. 10a) is shown in Fig. 9(f), which shows an improvement in χ^2 to ∼3.9. In both cases, the point-to-point ray tracing reveals a lack of model constraint in the lower crust in the vicinity of Marathon FZ and the outside corner (red stars in Fig. 9d) and a general paucity of sub-Moho sampling arrivals to the north of Marathon FZ.

Regardless of model definition, this ray tracing confirms that, to the north of Marathon FZ, observed first arriving phases are predominantly crustal Pg arrivals and that the variation in arrival time with offset is primarily a function of seabed topography as expected, and not significant lateral and vertical variation in apparent velocity to that expected for the mantle. The Pn arrivals (blue lines in Fig. 9e; green lines in Fig. 9f) observed to the south of Marathon FZ are shown to originate from shots only fired to its south. This modelling also shows that the gravity and seismic definitions of the interface geometries are also effectively equivalent within the pick uncertainties. On this basis the gravity interface definition is considered more likely since it produces the better fit to the FAA, coupled with it being the simpler of the two solutions (Occam's razor).

4.4.2 Moho

The apparent absence of PmP and Pn phases to the north of the Marathon FZ may indicate that a traditional distinct Moho interface may not exist with there being, instead, a transition zone from crust to mantle. Consequently, a forward predictive ray tracing approach, tracing all potential Pn and PmP arrivals through the model was also adopted, not only to test the appropriateness of the selected base of crust marker (7.5 km s^{-1} velocity contour), but also the likelihood that it is a distinct interface rather than a transition zone, and if so, where it exists. The forward model derived from the *density model* (henceforth known as the *velocity–depth model*) was used for this testing.

This process was undertaken in two ways: (i) tracing all possible Pn and PmP ray paths through the model—that is a predictive phase identification free approach and (ii) point-to-point ray tracing the

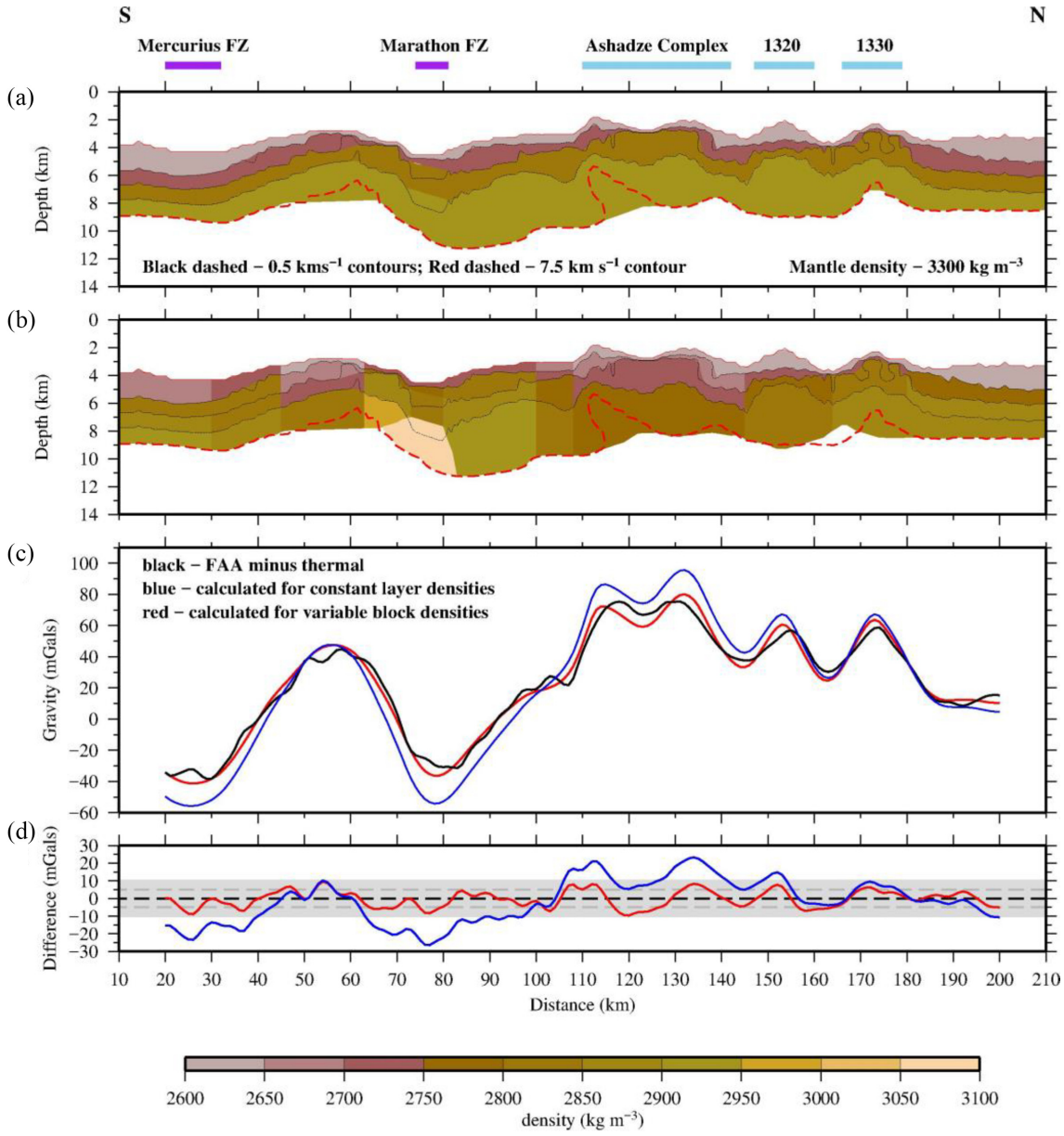

Figure 8. Uniqueness testing of the *inversion model* using the FAA. (a) Model obtained by converting the *inversion model* to density using 4.5, 5.5, 6.5 and 7.5 km s^{-1} velocity contours to define homogeneous density blocks, with densities ascribed using the relationship of Carlson & Raskin (1984). The red dashed line shows the 7.5 km s^{-1} velocity contour interpreted to mark the base of the crust in the *inversion model*. Although this model results in a good fit for the majority of the profile (blue line in c and d), notable misfits are observed in the vicinity of the fracture zones, Ashadze Complex and 1320 OCC (see annotation above). (b) Best-fitting *density model* obtained by subdividing the constant layer density model into a series of lateral blocks and adjusting the relative density. Note that the modelling reveals likely artefacts in the seismic model, and demonstrates that in the vicinity of Marathon FZ the crust is thinner and of a lower density, with a corresponding low-density region in the upper mantle. (c) Calculated FAA, colour-coded as annotated, and with the FAA corrected for along-axis thermal anomaly shown for comparison. (d) Misfit between calculated and observed anomalies, relative to the maximum FAA error of ±10 mGal (light grey shading), showing that the laterally variable density block model produces a fit within the error for the entire profile.

Pg arrival picks, reassigned as Pn phases instead—that is only those that satisfy a Pn pathway through the model would be traced. Six examples are shown in Fig. 10 for OBSs 6 (sited on the 1330 OCC), 8 (sited in between the 1320 and 1330 OCCs), 62 (sited on the north Ashadze Complex), 65 (sited on the southern edge of south Ashadze Complex), 68 (sited on the outside corner adjacent to Marathon FZ) and 70 (sited on ∼8 Ma inter-FZ crust).

This modelling confirmed firstly that phase assignments are valid, that Pn arrivals are only observed for OBSs located on crust to the south of Marathon FZ and that PmP arrivals are only observed to the south of Ashadze Complex and to the north of the 1330 OCC (i.e. for the ∼8 Ma crust captured between fracture zones and for the youngest crust of the eastern ridge flank respectively), with modelled PmP reflections mirroring phases observed on the record sections (Figs 10d and i) in these locations. The implication of this result is that, elsewhere, either a distinct Moho between crust and mantle is not present, instead it being a transition zone, or that the velocity contrast across the Moho is small, thus generating a PmP

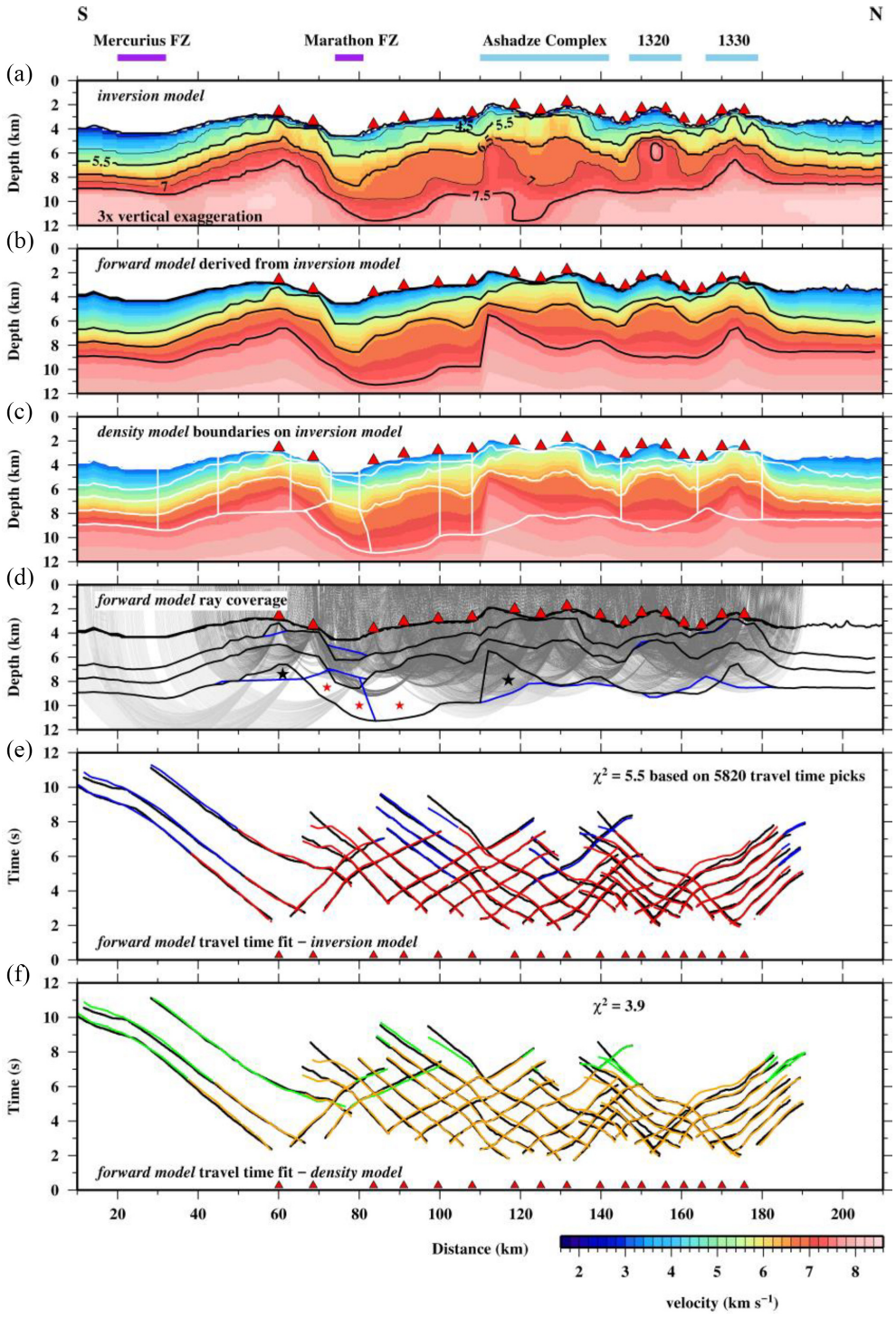

Figure 9. Model uniqueness and phase identification testing. (a) *Inversion model* with velocity contours plotted every 0.5 km s^{-1}. Prominent topographic features are annotated above. Red triangles in all parts show OBS locations. (b) *Forward model* derived from the *inversion model* using the 5.5, 6.5 and 7.5 km s^{-1} contours as interface boundaries, together with the seabed derived from the bathymetry. (c) *Density model* block boundaries plotted on the *inversion model*. (d) Forward modelling ray diagram calculated using a point-to-point approach as a check of phase identification of Pg (dark grey) and Pn (light grey) arrivals, and to appraise potential artefacts in the *inversion model*. Both the *inversion model*-derived interfaces (black) and *density model*-derived interfaces (blue) are traced. The areas of the *inversion model* marked by black stars are interpreted as artefacts of the inversion process. Areas marked by red stars show parts of the lower crust unconstrained by observed arrivals. Calculated traveltimes compared with the observed (black) for both the (e) inversion-derived (Pg—red; Pn—blue) model and (f) density-derived model (Pg—orange; Pn—green). The density-derived model results in a better fit within the pick errors (χ^2 annotated).

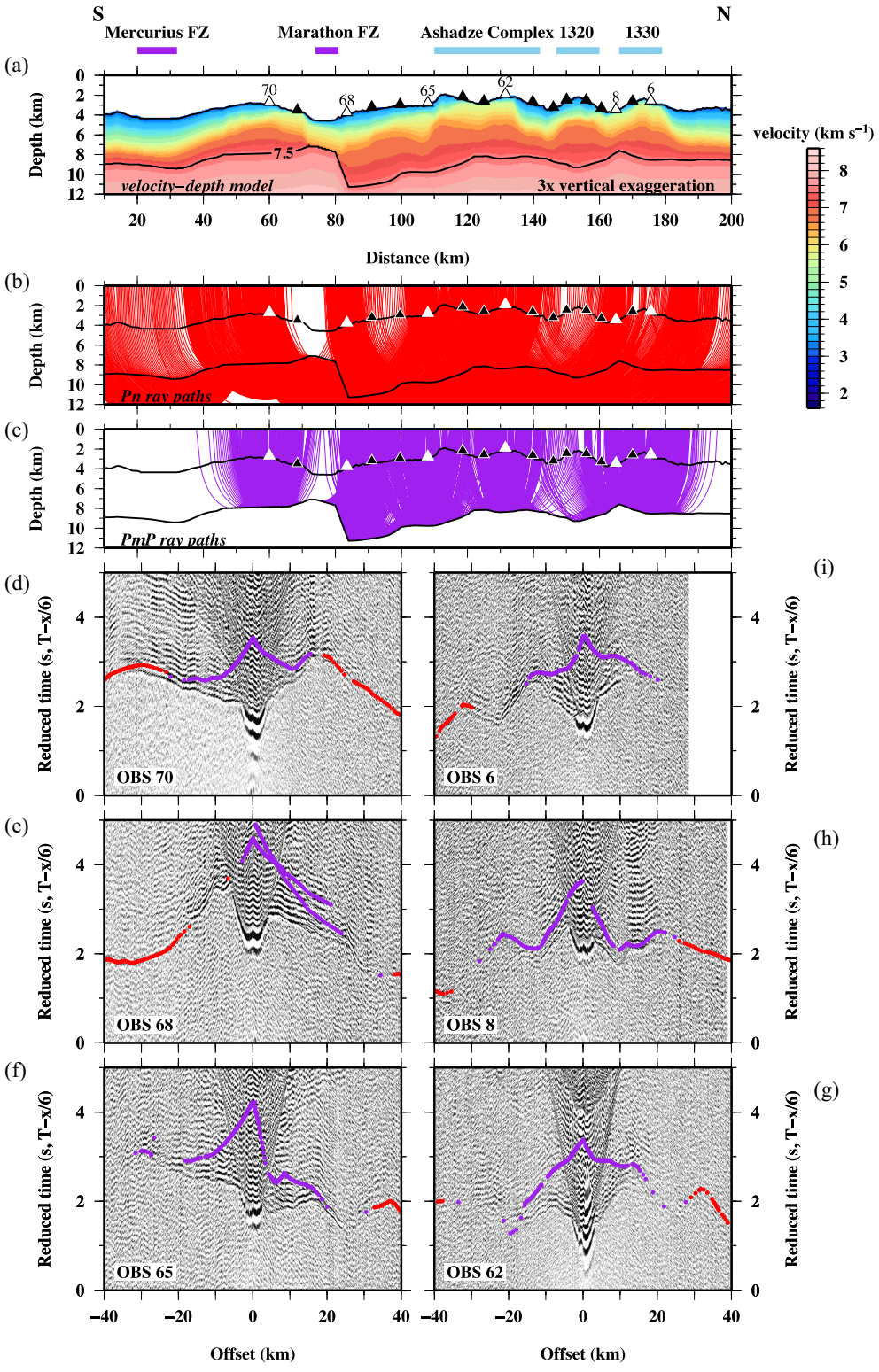

Figure 10. Forward ray trace prediction of Pn and PmP arrivals for Moho identification and characteristics. (a) Final *velocity–depth model*. OBS locations are shown by triangles, with the locations of those of the example record sections shown in d-i) highlighted in white. Six examples are chosen to reflect main tectonic region along-profile: OBSs 6 (sited on the 1330 OCC), 8 (sited in between the 1320 and 1330 OCCs), 62 (sited on the north Ashadze Complex), 65 (sited on the southern edge of south Ashadze Complex), 68 (sited on the outside corner adjacent to Marathon FZ), and 70 (sited on ∼8 Ma inter-FZ crust). Prominent topographic features are annotated above. Predictively traced (b) Pn (red) and (c) PmP (purple) ray paths calculated through the model in (a). Only the seabed and Moho interfaces are plotted. (d-i) Hydrophone record sections comparing calculated traveltimes against observed arrivals. All record sections are plotted filtered and reduced at 6 km s^{-1} and from south (d) to north (i). In general, this modelling, for all OBSs, shows that PmP arrivals are not unequivocally observed on the majority of record sections, except to the north of the 1330 OCC (i) and south of Marathon FZ (d), and that either the Moho is a transition zone, or if a first-order discontinuity, the velocity increase across it is small in amplitude.

arrival amplitude indistinguishable above that of the background noise. Consequently, the 7.5 km s^{-1} contour can be regarded as marking the base of the crust where a distinct Moho exists and also the top of a gradient transition into the mantle beneath all of the OCCs. Secondly, this modelling also suggests that, in the vicinity of Marathon FZ, the inversion modelling images the base of a zone of upper mantle serpentinisation, with a thinner and lower velocity crust above, beneath the width of transform fault zone, in comparison to that of the ∼1 Ma crust to the north and ∼8 Ma to the south.

4.4.3 Model features

On the basis of both the seismic and gravity forward modelling, the features of the *inversion model* were reappraised to identify which were a consequence of real geological structure and which result from the inversion process. The crustal thinning-like features centred at 60, 8 km (offset,depth) and 115, 8 km model space (Fig. 9d—black stars) were consequently interpreted as modelling artefacts, and the velocity increase 'bull's eye'-like structure beneath the 1320 OCC (Fig. 9a—152, 6 km model space) was considered to be a compensation, resulting from a gap in the ray coverage. However, the following were considered to be real crustal features:

(1) an oceanic crust that is ∼5 km thick;
(2) crustal thinning of ∼1 km in between the Ashadze Complex and the 1320 OCC;
(3) crustal thinning of ∼2 km between the 1320 and 1330 OCCs;
(4) higher velocity anomaly at shallower crustal depth beneath the breadth of the Ashadze Complex, except for the southern flank;
(5) higher velocity anomaly at shallower crustal depth beneath the 1330 OCC;
(6) higher velocity anomaly at mid-crustal depth beneath the 1320 OCC;
(7) thicker overall crust, resulting largely from a thicker lower crust, to the north of the Marathon FZ beneath the outside corner;
(8) a thinner, lower velocity crust within Marathon FZ underlain by a serpentinized uppermost mantle and
(9) sharp transition to an average crustal thickness to the south of the Marathon FZ, that corresponds to the southern edge of the bathymetric deep.

5 VELOCITY–DEPTH MODEL CONSIDERATION

To demonstrate the variation along-axis in crustal velocity–depth structure, a set of 1-D profiles (Fig. 11) was extracted every 5 km from the *velocity–depth model* containing gravity modelling-derived interface adjustments (Fig. 10a) and referenced relative to the seabed since there is little-to-no sediment cover. These profiles reveal the average crustal thickness to be ∼5 km, and that the velocity–depth profiles vary when compared to the standard Atlantic oceanic envelope of White *et al.* (1992), and the compilation of Grevemeyer *et al.* (2018b). For the purpose of model interpretation, we further divide the profiles into the primary tectonic domains of: (i) 8 Ma inter-fracture zone crust south of Marathon FZ (Fig. 11a); (ii) outside corner (Fig. 11b); (iii) Ashadze Complex (Fig. 11c); (iv) the 1320 OCC (Fig. 11d); (v) the 1330 OCC (Fig. 11e) and (vi) 0–1 Ma crust of the eastern ridge-flank (Fig. 11g).

5.1 8 Ma inter-fracture zone crust–0–70 km along-model distance

Although least well constrained by the seismic modelling, the crust to the south of Mercurius FZ is seen to be ∼5 km thick, consisting of an ∼2-km-thick upper and middle crust (3.0–4.5 km s^{-1}), and a 3-km-thick lower crust that reaches 7.5 km s^{-1} at the Moho, where the depth to this boundary is constrained by Pn arrivals. If the 7.5 km s^{-1} velocity contour is used to denote the base of crust, the uppermost mantle velocity is also relatively slow, at 7.6–7.8 km s^{-1}, when compared to the typical Atlantic crustal envelopes (White *et al.* 1992; Grevemeyer *et al.* 2018b). However, within ∼10 km of Marathon FZ (pink profiles in Fig. 11a), in what would have been an inside corner position when this crust was at the spreading ridge, higher velocities are observed at shallower depth sub-seabed that correspond to higher densities (Fig. 8b) and a shallowing of the base of the crust on the southernmost flank of Marathon FZ. The velocity–depth profiles of the southern flank of Marathon FZ are similar to those of 1330 and north Ashadze Complex OCCs. Therefore, the crust between 60 and 70 km model offset, although formed in an inside corner high position, appears to have OCC-like characteristics.

The bathymetry of the inside corner shows the presence of large faults similar to those observed at the Rainbow vent site on the MAR further to the north (e.g. Dunn *et al.* 2017 and references therein), where they are interpreted to result from block rotation and crustal thinning, forming ridge-parallel bands. However, crustal thinning is not observed between Marathon and Mercurius FZ in the 13°N MAR setting.

5.2 Marathon FZ—70–80 km along-model distance

Within Marathon FZ a region of lower velocity exists beneath the width of the FZ that extends throughout the crust (Fig. 10a), most likely indicative of a fractured zone rather than a single fault system. The primary evidence for a thinner crust beneath the surface expression of the Marathon FZ comes from the gravity modelling, which suggests a lower density zone ∼2–3 km-deep and ∼20 km-wide exists in the upper mantle most likely representing serpentinized peridotite (Fig. 8b), resulting from the ingress of sea water through the fracture zone fault system.

5.3 Outside corner—80–100 km along-model distance

The outside corner appears to be marked by a 2–3 km increase in crustal thickness, and a crustal velocity–depth profile similar to that of regions without OCCs. Gravity modelling (Fig. 8b) suggests a similar density–depth profile to that of the outside corner of Mercurius FZ (model distance ∼30–40 km), although the crust there is, on average, ∼5 km thick. The southward-dipping geometry of the contours, together with the arcuate-upwards pattern of MCS reflectors within both FZs (Figs 3c and d), suggests that the outside corner regions of both FZ-ridge intersections have undergone relative uplift, and that the lithosphere captured between FZs is similarly being uplifted towards the north. The arcuate-upwards reflectors within the northern side of the Marathon FZ valley also suggest that, as yet, this fracture zone is not entirely locked, or the lithospheres to the north and south are not rigidly coupled, despite being ∼10–15 km from the current transform nodal deep/spreading ridge tip.

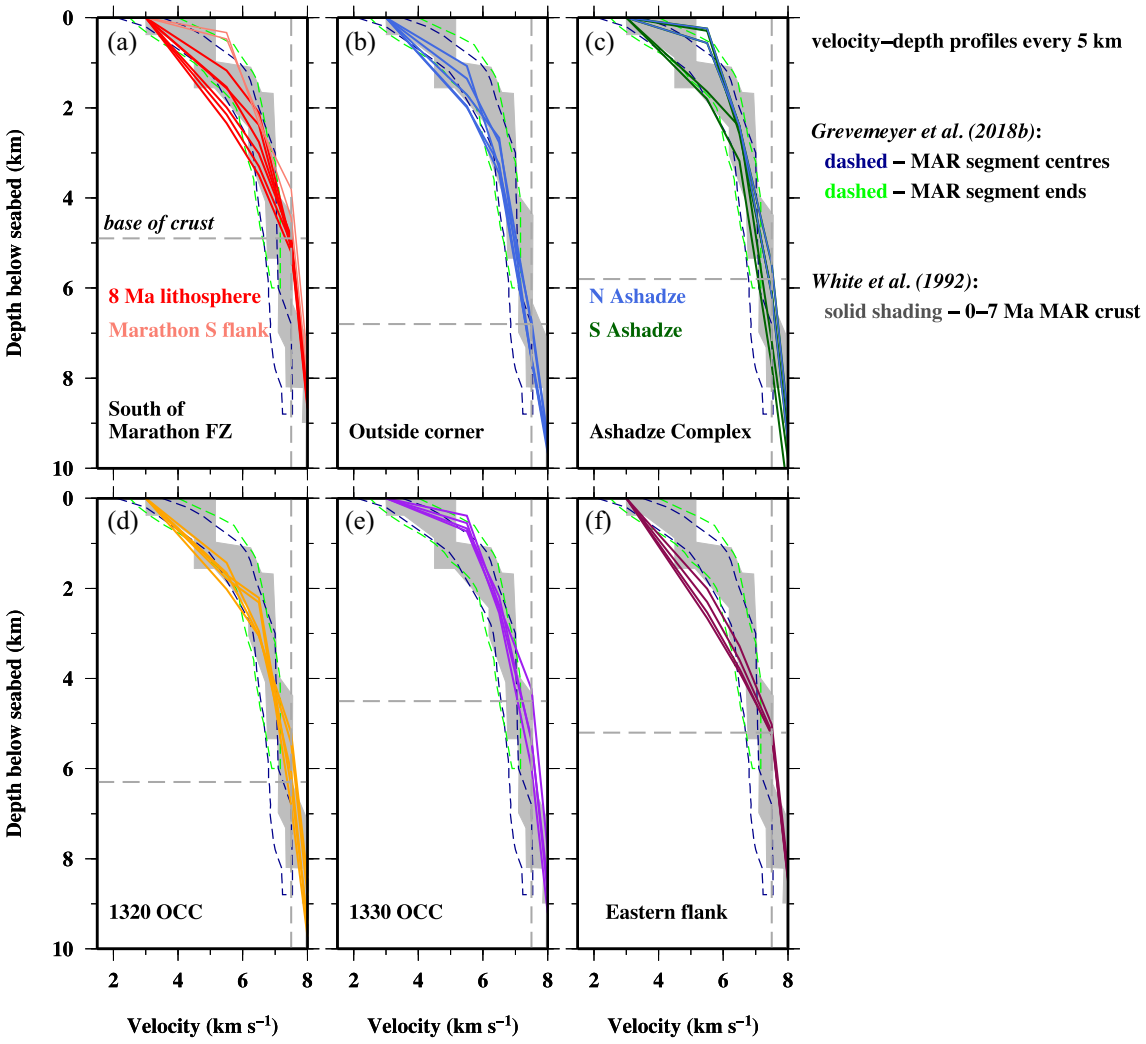

Figure 11. Comparison of crustal velocity–depth structure along-profile. 1-D velocity–depth profiles, extracted at 5 km intervals through the *velocity–depth model* (Fig. 10a), are colour-coded with respect to setting along-profile in all parts. (a–f) Velocity–depth profiles plotted relative to seabed depth, highlighting the range in crustal thickness (horizontal grey dashed lines), and compared to the standard Atlantic crustal velocity–depth envelopes of White *et al.* (1992) (grey = 0–7 Ma MAR crust) and Grevemeyer *et al.* (2018b) (blue dashed = MAR segment centre crust; green dashed = MAR segment end crust). Velocity–depth profiles are shown separately for the main tectonic domains identified along-profile as annotated.

5.4 Western ridge-flank OCC crust—100–185 km along-model distance

Each of the OCCs traversed show an elevated velocity at shallow levels within the crust with, in the case of the north Ashadze Complex (Fig. 11c) and 1330 OCC (Fig. 11e), velocities as high as 5.5 km s^{-1} at shallowest sub-seabed depths, implying that these OCCs are predominantly underlain by lower crustal rocks or serpentinized ultramafic lithologies. However, beneath the 1320 OCC (Fig. 11d) and to a lesser extent the south Ashadze Complex (Fig. 11c), the velocity–depth structure suggests that the upper crust is still predominantly comprised of more basaltic-type lithologies, although these are thinner than would be expected for a normal oceanic crustal succession. The *density model* (Fig. 8b) also supports this conclusion, especially so for the 1320 OCC, which shows a thickness of 2600 kg m^{-3} material beneath the seabed similar to that of the crust of the eastern flank that is viewed to have been formed by magmatic accretion (e.g. MacLeod *et al.* 2009).

These contrasting velocity patterns (Fig. 10a) may reflect the differing tectonic settings in which Profile R crosses each OCC—close to the centre of the exposed detachment fault of the Ashadze Complex, at the breakaway at 1320 OCC, and just after breakaway at 1330 OCC. Alternatively, they may suggest that a greater degree of lower crust/upper mantle exhumation has occurred at the north Ashadze Complex and 1330 OCCs than at the south Ashadze Complex, or that in these settings a greater degree of serpentinization has occurred. The only vent field in close proximity to Profile R is Semyenov (its lateral position is marked on Fig. 6c). Although 0.76 km off-profile, and considering the three-dimensionality of the seabed and the feature scale resolution of the velocity model at shallow crustal depth, there is no apparent low velocity or low density anomaly associated with this feature that might constrain a heat source. Instead, it is underlain by a region of higher velocity than the immediate surrounds, similar to that observed beneath the active OCC Mt Dent-hosted vent system at the MCSC (Harding *et al.* 2017; van Avendonk *et al.* 2017).

Perhaps the more interesting feature of the *velocity–depth model* (Fig. 10a) is the steepness in depth change of velocity between OCCs, in particular between the north Ashadze Complex and the 1320 OCC and at the northern edge of the 1330 OCC, which is observed from the seabed to the Moho. This pattern is mirrored in the *density model*, which provides further constraint on the crustal thickness variation between the 1320 and 1330 OCCs, in between which the crust thins by ∼2 km. This distinction, and the contrasting shallow crustal structures, suggests that these OCCs are most likely independent and tectonically isolated features. This suggestion is supported by the pattern of magnetization (Searle et al., 2016, 2018), and by the pattern of microseismicity (Parnell-Turner *et al.* 2017), with the deeper events nominally beneath the 1330 OCC and the shallower ones beneath the 1320 OCC. The velocity–depth profiles (Fig. 11b) from the northerly part of the outside corner also share similar characteristics of those of the older/relic OCCs.

5.5 Eastern ridge-flank crust—185–210 km along-model distance

Beneath the eastern ridge flank the ∼1-Myr-old oceanic crust is ∼6 km thick and displays a similar velocity–depth profile to that observed for the oldest crust in the vicinity of the Mercurius FZ. Although this region has the least seismic constraint along the model, gravity modelling suggests the velocity–depth profile observed just to the north of the 1330 OCC can be extended to the northern end of Profile R. A distinct Moho reflection is observed to the north of the 1330 OCC (Fig. 10i), and suggests that the crust here, although thin, is of a more standard structure and probably represents a region undergoing a phase of predominantly magma-rich formation, as evidenced by the variety of magmatic constructs at the seabed (Fig. 2), magnetic anomaly modelling (Searle et al., 2016, 2018) and the general attenuation in seismic signal amplitude observed for shots fired to the north of the 1330 OCC (Figs 4a, b and 10g–i). The FAA and RMBA (Figs 5c and d) and, to a lesser extent, magnetic anomaly (Fig. 5e) also suggest a different crustal style in this region, in particular suggesting that the deviation in ridge axis linear trend here, described by Mallows & Searle (2012) as a non-transform offset, may now be in the incipient stages of transition to a transform offset. Where not hosting OCCs, the crust of the 13°N region, in general, appears to display a simple velocity gradient structure from seabed to Moho, and a distinct Moho interface marking the base of the crust.

6 POTENTIAL FIELDS

As a means of understanding the across-axis context of the 2-D ridge-parallel Profile R interpretation, the gravity and magnetic anomalies were investigated further using the data acquired throughout JC102, JC109 and JC132. Fig. 5 shows a comparison between the seabed bathymetry (Fig. 5a), free-air anomaly (FAA—Fig. 5c), residual mantle Bouguer anomaly (RMBA—Fig. 5d), total field magnetic anomaly (TFMA—Fig. 5e) and the reduced to pole magnetic anomaly (Fig. 5f).

The bathymetry and FAA together clearly show the asymmetry in across-ridge spreading-related topography with linear, north-south-trending significant bathymetric highs separated by ∼24 km in the flow line direction between ridge flanks, which equates to a time frame of ∼2 Myr at a half spreading rate of ∼12 mm yr^{-1}. These features, observed off-axis on the eastern ridge flank, lie in locations that mirror the gaps between extant OCCs in the western ridge flank. The RMBA on the other hand shows a relative gravity low to the north of the 1330 OCC consistent with, although now better defined, that observed by Smith *et al.* (2008) and Mallows & Searle (2012). RMBA anomalies at mid-ocean ridges are interpreted to reflect either or both density variation in the crust or mantle, with lows equated to higher temperature magma-rich conditions with or without a correspondingly thicker crust. For a suite of adjacent OCCs, exhuming lower crustal and uppermost mantle rocks to shallower levels, there should be an associated RMBA high, with a surrounding relative low elsewhere, associated with normally accreted crust.

The TFMA should reveal regions of magmatic accretion during the current epoch (positive anomaly) or, conversely, regions where basalt rocks are replaced in the near-surface or at the seabed by those of the lower crust and upper mantle. In Figs 5e and f, positive regions in the vicinity of the ridge axis most likely equate to places where magma-rich formation is currently on-going, while negative anomalies equate to actively evolving mature OCCs (Searle et al., 2016, 2018). On this basis, the TFMA and reduced to pole magnetic anomaly suggest that magmatism may have initiated in the axial region to the west of the toe of the 1320 OCC while, for the 1330 OCC, magmatic accretion may have initiated within and surrounding it.

Perhaps the most interesting observation lies to the north of the 1330 OCC (180–200 km along profile distance), where a pair of deep TFMA lows (Fig. 5e) and a corresponding low in the RMBA (Fig. 5c), both marked by crosses in Fig. 5, suggest that the non-transform discontinuity previously interpreted at this location may have evolved from a deviation in ridge linear trend into a small offset transform discontinuity. As a consequence, the 1330 OCC may be undergoing rifting ∼20 km behind (west of) the seabed emergence of the detachment surface, perhaps due to an active ridge tip propagating southward.

7 CONCLUSIONS

This ridge-parallel study of the 13°N segment of the MAR aimed to investigate the crustal structure and inter-relationships between OCCs, extending the results of a tomographic study of the 1320 OCC (Simão *et al.* 2016 and forthcoming Simão *et al.* 2018) to the north and south, to investigate along axis connectivity of the detachment fault, and to better understand any relationship to the adjacent segment bounding fracture zones to the south and the now thought-to-be transform ridge axis discontinuity, mid-segment to the north. From our study, we draw the following conclusions:

(1) Both the seismic and gravity models presented in this paper reveal distinct crustal structures between the OCCs currently in the vicinity of the western flank of the ridge axis, but with each showing varying degrees of elevated velocity at shallow subseabed depth, and contrasting density structures.

(2) The magnetic anomaly, coupled with observations of neovolcanic features on the seabed and attenuation of seismic arrivals, suggests that magmatism may have initiated in the axial region to the west of the toe of the 1320 OCC while, for the 1330 OCC, magmatism may have initiated within and surrounding it.

(3) The along-axis variation in velocity and density suggests that each OCC is structurally distinct and is exhumed along its own detachment fault, the boundary between which is marked by a thinner crust. For the Ashadze Complex and 1330 OCCs the velocity model suggests these detachments have exhumed rocks of the lower crust or serpentinized ultramafic lithologies to the seabed within the footwall, while for the 1320 OCC, the velocity and density models suggest that the upper crust comprises mainly basaltic-lithologies

despite the reported exposures of gabbros and serpentinites (Escartin *et al.* 2017).

(4) The results of our combined modelling of wide-angle seismic and gravity data, and comparison of the resulting models with the swath bathymetry and magnetic anomaly, favours the *Localized* model of OCC evolution in which OCCs are spatially restricted, structurally isolated and ephemeral features that are switched on and off by variations in magma-rich and magma-poor ridge-axis conditions. However, it should be noted that the two closely spaced OCCs of the Ashadze Complex appear to exhibit similar crustal structures at depth, such that they may now be linked, although the north and south sections have quite distinct shallow crustal velocity and density profiles.

(5) The outside corner to the north of the Marathon FZ shows, although to a lesser extent, elevated velocity at shallower depth in a pattern not dissimilar to that observed beneath an OCC.

(6) The pattern of intrasediment reflectivity within the Marathon and Mercurius FZs suggests that neither became locked immediately on transform-to-fracture transition. As the crust to the north of Marathon FZ still appears to be undergoing uplift relative to the crust on the opposite side, our results suggest that movement does occur across fracture zones at least until ∼1 Myr after transition, this being the point at which we have imaged it. The older Mercurius FZ to the south, although apparently now locked, also appears to have accommodated a phase of northern relative uplift.

(7) Based on gravity modelling, Marathon FZ appears to have a thin, lower velocity crust that is contained to within its bathymetric footprint. Beneath the crust, a 2–3-km-deep, ∼20-km-wide zone of lower density appears to suggest a serpentinized upper mantle.

(8) The magmatism in the vicinity of the 1330 OCC, and its apparent incipient dissection, may be associated with ridge tip southern propagation and readjustment of ridge geometry along-axis, with a corresponding evolution of a deviation in ridge linear trend into a small-offset transform discontinuity.

ACKNOWLEDGEMENTS

This research project was funded by the Natural Environmental Research Council (NERC) grants NE/J02029X/1, NE/J022551/1 and NE/J021741/1. We would like to thank all involved in the planning and acquisition of data during research cruise JC132 (Reston & Peirce 2016), including the officers, engineers and crew of the RRS James Cook, the scientific party, and all seagoing technicians. The NERC Ocean-Bottom Instrumentation Facility (Minshull *et al.* 2005) provided the OBSs used in this project, together with their technical support at sea. The MCS data were processed using Claritas™ and manipulated for plotting using Seismic Unix. All figures were prepared using the Generic Mapping Tools (GMT) package (Wessel & Smith 1998). All data from cruises JC102, JC109 and JC132 are archived at the NERC's British Oceanographic Data Centre (www.bodc.ac.uk), and the final accepted version of this manuscript is available through Durham Research Online (dro.dur.ac.uk). We thank the three reviewers for their comments.

REFERENCES

Baines, A.G., Cheadle, M.J., John, B.E. & Schwartz, J.J., 2008. The rate of detachment faulting at Atlantis Bank, SW Indian Ridge, *Earth planet. Sci. Lett.,* **273,** 105–144.

Beltenev, V. *et al.*, 2007. A new hydrothermal field at 13°30'N on the Mid-Atlantic Ridge, *InterRidge News,* **16,** 10–11.

Blackman, D.K. & Collins, J.A., 2010. Lower crustal variability and the crust/mantle transition at the Atlantis Massif oceanic core complex, *Geophys. Res. Lett.,* **37,** L24303.

Blackman, D.K. & Forsyth, D.W., 1991. Isostatic compensation of tectonic features of the Mid-Atlantic Ridge: 25–27°30'S, *J. geophys. Res.,* **96,** 11,741–711,758.

Blackman, D.K., Karson, J. & Kelley, D.S. and the Scientific Party, 2001. Seafloor mapping and sampling of the MAR 30° N oceanic core complex - MARVEL (Mid-Atlantic ridge vents in extending lithosphere), *InterRidge News,* **10,** 33–36.

Blackman, D.K. *et al.*, 2006. Oceanic core complex formation, Atlantis Massif; Expedition 304 and 305 of the riserless drilling platform from and to Ponta Delgada, Azores (Portugal), Sites U1309-1311, *Proceedings of the Integrated Ocean Drilling Program,* **304/305,** doi:10.2204/iodp.proc.304305.2006.

Blackman, D.K. *et al.*, 2011. Drilling constraints on lithospheric accretion and evolution at Atlantis Massif, Mid-Atlantic Ridge 30 degrees N, *J. geophys. Res.,* **116,** B07103.

Bonatti, E., 1976. Serpentine protrusions in the oceanic crust, *Earth planet. Sci. Lett.,* **32,** 107–113.

Bonatti, E., 1978. Vertical tectonism in oceanic fracture zones, *Earth planet. Sci. Lett.,* **37,** 369–379.

Bortnikov, N.S., Simonov, V.A., Borovikov, A.A., Bel'tenev, V.E., Amplieva, E., Kotlyarov, A.V. & Bryanskiy, N.V., 2015. The metalliferous fluid of the hydrothermal sulfide system associated with the oceanic core complex 13°20'N: the Mid-Atlantic Ridge (LA-ICP-MS and fluid inclusions), in *Oceanic Core Complexes and Hydrothermalism, Russian Ridge 2105 Workshop Program,* pp. 80–83, Moscow, Russia.

Canales, J.P., 2010. Small-scale structure of the Kane Oceanic Core Complex, Mid-Atlantic Ridge 23°30'N, from waveform tomography of multichannel seismic data, *Geophys. Res. Lett.,* **37,** L21305.

Canales, J.P., Detrick, R.S., Lin, J., Collins, J.A. & Toomey, D.R., 2000. Crustal and upper mantle seismic structure beneath the rift mountains and across a non-transform offset at the Mid-Atlantic Ridge (35° N), *J. geophys. Res.,* **105,** 2699–2719.

Canales, J.P., Dunn, R.A., Arai, R. & Sohn, R.A., 2017. Seismic imaging of magma sills beneath an ultramafic-hosted hydrothermal system, *Geology,* **45,** 447–450.

Canales, J.P., Tucholke, B.E. & Collins, J.A., 2004. Seismic reflection imaging of an oceanic detachment fault: Atlantis megamullion (Mid-Atlantic Ridge, 30°10'N), *Earth planet. Sci. Lett.,* **222,** 543–560.

Canales, J.P., Tucholke, B.E., Xu, M., Collins, J.A. & DuBois, D.L., 2008. Seismic evidence for large-scale compositional heterogeneity of oceanic core complexes, *Geochem. Geophys. Geosyst.,* **9**(8), doi: 10.1029/2008GC002009.

Cann, J.R. & Smith, D.K., 2005. Evolution of volcanism and faulting in a segment of the Mid-Atlantic Ridge at 25° N, *Geochem. Geophys. Geosyst.,* **6,** doi:10.1029/2005gc000954.

Cann, J.R. *et al.*, 1997. Corrugated slip surfaces formed at ridge-transform intersections on the Mid-Atlantic Ridge, *Nature,* **385,** 329–332.

Carlson, R.L. & Raskin, G.S, 1984. Density of the oceanic crust, *Nature,* **311,** 555–558.

Cherkashev, G.A. *et al.*, 2013. Massive sulfide ores of the northern equatorial Mid-Atlantic Ridge, *Oceanol.,* **53**(5), 607–619.

Cherkashov, G., Kuznetsov, V., Kuksa, K., Tabuns, E., Maksimov, F. & Bel'tenev, V., 2016. Sulfide geochronology along the northern equatorial Mid-Atlantic Ridge, *Ore Geol. Rev.,* doi:10.1016/j.oregeorev.2016.10.015.

Cherkashov, G., Lazareva, L. & Stepanova, T., 2010a. Massive sulfide deposits at Semyenov cluster: mineralogy, age and evolution, *Miner. Ocean Deep Miner. Min, Joint International Meeting, St. Petersbourg, Russia,* 52–57.

Cherkashov, G. *et al.*, 2008. Two new hydrothermal fields at the Mid-Atlantic Ridge, *Mar. Geores. & Geotech.,* **26**(4), 308–316.

Cherkashov, G. *et al.*, 2010b. Seafloor massive sulfides from the northern equatorial Mid-Atlantic Ridge: new discoveries and perspectives, 33rd International Geological Congress (IGC), Oslo, Norway, *Mar. Geores. & Geotech.,* **28**(3), PII 926309106, 222–239.

Choi, E. & Buck, W.R., 2012. Constraints on the strength of faults from the geometry of rider blocks in continental and oceanic core complexes, *J. geophys. Res.,* **117,** B04410.

Collette, B.J., 1974. Thermal contraction joints in a spreading seafloor as origin of fractures zones, *Nature,* **251,** 299–300.

Collins, J.A., Smith, D.K. & McGuire, J.J., 2012. Seismicity of the Atlantis Massif detachment fault, 30° N at the Mid-Atlantic Ridge, *Geochem. Geophys. Geosyst.,* **13,** Q0AG11.

Combier, V., Seher, T., Singh, S.C., Crawford, W.C., Cannat, M., Escartín, J. & Dusunur, D., 2015. Three-dimensional geometry of axial magma chamber roof and faults at Lucky Strike volcano on the Mid-Atlantic Ridge, *J. geophys. Res.,* **120,** 5379–5400.

Cormier, M.H., Detrick, R.S. & Purdy, G.M., 1984. Anomalously thin crust in oceanic fracture zones - new seismic constraints from the Kane fractur zone, *J. geophys. Res.,* **89**(B12), 249–266.

Dannowski, A., Grevemeyer, I., Ranero, C.R., Ceuleneer, G., Maia, M., Morgan, J.P. & Gente, P., 2010. Seismic structure of an oceanic core comples at the Mid-Atlantic Ridge, 22°19'N, *J. geophys. Res.,* **87,** doi:10.1029/2009JB006943.

Dannowski, A., Morgan, J.P, Grevemeyer, I. & Ranero, C.R., 2018. Enhanced mantle upwelling/melting cause segment propagation, oceanic core complex die off, and the death of a transform fault: the Mid-Atlantic Ridge at 21.5° N, *J. geophys. Res.,* **123,** 941–856.

deMartin, B.J., Sohn, R.A., Canales, J.P. & Humphris, S.E., 2007. Kinematics and geometry of active detachment faulting beneath the Trans-Atlantic Geotraverse (TAG) hydrothermal field on the Mid-Atlantic Ridge, *Geology,* **35**(8), 711–714.

Detrick, R., White, R. & Purdy, G., 1993. Crustal structure of north-Atlantic fracture-zones, *Rev. Geophys.,* **31**(4), 439–458.

Detrick, R.S & Purdy, G.M., 1980. The crustal structure of the Kane fracture zone from seismic refraction studies, *J. geophys. Res.,* **85**(B7), 3759–3777.

Detrick, R.S., Cormier, M.H., Prince, R.A., Forsyth, D. & Ambos, E.L., 1982. Seismic constraints on the crustal structure within the Vema fracture zone, *J. geophys. Res.,* **87**(B13), 599–612.

Dick, H.J.B., Tivey, M.A. & Tucholke, B.E., 2008. Plutonic foundation of a slow-spreading ridge segment: oceanic core complex at Kane megamullion, 23°30'N, 45°20'W, *Geochem. Geophys. Geosyst.,* **9,** Q05014.

Dunn, R.A., Arai, R., Eason, D.E., Canales, J.P. & Sohn, R.A., 2017. Three-dimensional seismic structure of the Mid-Atlantic Ridge: An investigation of tectonic, magmatic, and hydrothermal processes in the Rainbow area, *J. geophys. Res.,* **122**(12), 9580–9602.

Escartin, J. & Canales, J.P., 2011. Detachments in oceanic lithosphere: deformation, magmatism, fluid flow, and ecosystems, *EOS, Trans. Am. geophys. Un.,* **92,** 31.

Escartin, J. *et al.*, 2017. Tectonic structure, evolution, and the nature of oceanic core complexes and their detachment fault zones (13 degrees 20'N and 13 degrees 30'N, Mid Atlantic Ridge), *Geochem. Geophys. Geosyst.,* **18**(4), 1451–1482.

Escartın, J., Smith, D.K., Cann, J., Schouten, H., Langmuir, C.H. & Escrig, S., 2008. Central role of detachment faults in accretion of slow-spreading oceanic lithosphere, *Nature,* **455,** 790–794.

Escartın, J.C., Mevel, C., MacLeod, C.J. & McCaig, A.M., 2003. Constraints on deformation conditions and the origin of oceanic detachments: the Mid-Atlantic ridge core complex at 15°45'N, *Geochem. Geophys. Geosyst.,* **4**(8).

Forsyth, D.W. & Wilson, B., 1984. Three dimensional temperature structure of a ridge-transform-ridge system, *Earth planet. Sci. Lett.,* **70,** 355–362.

Fox, P.J., Scheiber, E., Rowlett, H. & McCamy, K., 1976. Geology of Oceanographer fracture zone – model for fractures zones, *J. geophys. Res.,* **81**(23), 4117–4128.

Frueh-Green, G.L. *et al.*, 2016. International Ocean Discovery Program Expedition 357 Preliminary Report: Atlantic Massif serpentinization and life, *Int. Ocean Disc. Prog.,* doi:10.14379/iodp.pr.357.2016.

Grevemeyer, I., Hayman, N.W., Peirce, C., Schwardt, M., Van Avendonk, H.J.A., Dannowski, A. & Papenberg, C., 2018a. Episodic magmatism and serpentinised mantle exhumation at an ultraslow-spreading centre, *Nat. Geosci.,* doi:10.1038/s41561-018-0124-6.

Grevemeyer, I., Ranero, C.R. & Ivandic, M., 2018b. Structure of oceanic crust and serpentinisation at subduction trenches, *Geosphere,* **14**(2), 1–23.

Grimes, C.B., John, B.E., Cheadle, M.J. & Wooden, J.L., 2008. Protracted construction of gabbroic crust at a slow spreading ridge: constraints from 206 Pb/238U zircon ages from Atlantic Massif and IODP hole U1309D (30° N, MAR), *Geochem. Geophys. Geosyst.,* **9,** doi:10.1029/2008GC002063.

Harding, A.J., Arnulf, A.F. & Blackman, D.K., 2016. Velocity structure near IODP Hole U1309D, Atlantis Massif, from waveform inversion of streamer data and borehole measurements, *Geochem. Geophys. Geosyst.,* **17,** doi:10.1002/2016GC006312.

Harding, J.L., Van Avendonk, H.J.A., Hayman, N.W., Grevemeyer, I., Peirce, C. & Dannowski, A., 2017. Magmatic-tectonic conditions for hydrothermal venting on an ultraslow-spread oceanic core complex, *Geology,* **45**(9), 839–842.

Hayman, N.W., Grindlay, N.R., Perfit, M.R., Mann, P., Leroy, S. & de Lépinay, B.M., 2011, Oceanic core complex development at the ultraslow spreading Mid-Cayman spreading centre, *Geochem. Geophys. Geosyst.,* **12**(3), doi:10.1029/2010GC003240.

Henig, A.S., Blackman, D.K., Harding, A.J., Canales, J.-P. & Kent, G.M., 2012. Downward continued multi-channel seismic refraction analysis of Atlantis Massif oceanic core complex, 30° N Mid-Atlantic Ridge, *Geochem. Geophys. Geosyst.,* **13,** Q0AG07.

Hooft, E.E.E., Detrick, R.S., Toomey, D.R., Collins, J.A. & Lin, J., 2000. Crustal and upper mantle structure along three contrasting spreading segments of the Mid-Atlantic Ridge, 33.5°-35° N, *J. geophys. Res.,* **105,** 8205–8226.

Hosford, A., Lin, J. & Detrick, R.S., 2001. Crustal evolution over the last 2 m.y. at the Mid-Atlantic Ridge OH-1 segment, 35° N, *J. geophys. Res.,* **106**(B7), 13269–13285.

Hussenoeder, S.A., Kent, G.M. & Detrick, R.S., 2002. Upper crustal seismic structure of the slow spreading Mid-Atlantic Ridge, 35° N: Constraints on volcanic emplacement processes, *J. geophys. Res.,* **107**(B8), 2156.

Ildefonse, B. *et al.*, 2007. Oceanic core complexes and crustal accretion at slow-spreading rates, *Geology,* **35,** 623–626.

Karson, J.A., Frueh-Green, G.L., Kelley, D.S., Williams, E.A., Yoerger, D.R. & Jakuba, M., 2006. Detachment shear zone of the Atlantic Massif core complex, Mid-Atlantic Ridge, 30° N, *Geochem. Geophys. Geosyst.,* **7,** Q06016.

Lagabrielle, Y., Mamaloukas-Frangoulis, V., Cannat, M., Auzende, J.-M., Honnorez, J., Mevel, C. & Bonatti, E., 1992. Vema Fracture Zone (central Atlantic):- Tectonic and magmatic evolution of the median ridge and the eastern ridge-transform intersection domain, *J. geophys. Res.,* **97**(B12), 17331–17351.

Ludwig, W.J. & Rabinowitz, P.D., 1980. Structure of the Vema fracture zone, *Mar. Geol.,* **35**(1-3), 99–110.

MacLeod, C.J., Carlut, J., Escartin, J., Horen, H. & Morris, A., 2011. Quantitative constraint on footwall rotations at the 15°45'N oceanic core complex, Mid-Atlantic Ridge: implications for oceanic detachment fault processes, *Geochem. Geophys. Geosyst.,* **12,** Q0AG03.

MacLeod, C.J., Searle, R.C., Casey, J.F., Murton, B.J., Mallows, C., Unsworth, S.C., Achenbach, K.L. & Harrisc, M., 2009. Life cycle of oceanic core complexes, *Earth planet. Sci. Lett.,* **287,** 333–344.

MacLeod, C.J. *et al.*, 2002. Direct geological evidence for oceanic detachment faulting: the Mid-Atlantic Ridge, 15°45'N, *Geology,* **30,** 879–882.

Mallows, C & Searle, R.C., 2012. A geophysical study of oceanic core complexes and surrounding terrane, Mid-Atlantic Ridge at 13°-14° N, *Geochem. Geophys. Geosyst.,* **13,** Q06016.

Minshull, T.A., Morris, E. & Detrick, R.S., 1995. Gravity anomalies and crustal structure at the Mesozoic Blake Spur fracture zone, *J. geophys. Res.,* **100**(B9), 17,771–717,779.

Minshull, T.A., Sinha, M.C. & Peirce, C., 2005. Multi-disciplinary, subseabed geophysical imaging: a new pool of 28 seafloor instruments in use by the United Kingdom Ocean Bottom Instrument Consortium, *Sea Technol.,* **46,** 27–31.

Minshull, T.A., White, R.S., Mutter, J.C., Buhl, P., Detrick, R.S., Williams, C.A. & Morris, E., 1991. Crustal structure at the Blake Spur fracture zone from expanding spread profiles, *J. geophys. Res.,* **96,** 9955–9984.

Mitchell, N.C., Allerton, S. & Escartin, J., 1998. Sedimentation on young ocean floor at the Mid-Atlantic Ridge, 29° N, *Mar. Geol.,* **148**(1-2), 1–8.

Morris, A.R., Gee, J.S., Pressling, N.J., Johnc, B.E., MacLeod, C.J., Grimes, C.B. & Searlef, R.C., 2009. Footwall rotation in an oceanic core complex quantified using reorientated Integrated Ocean Drilling Program core samples, *Earth planet. Sci. Lett.,* **287,** 217–228.

Mutter, J.C. & Karson, J.A., 1992. Structural processes at slow-spreading ridges, *Science,* **257,** 627–634.

Müller, M.R., Minshull, T.A. & White, R.S., 2000. Crustal structure of the Southwest Indian Ridge at the Atlantis II fracture zone, *J. geophys. Res.,* **105**(B11), 25809–25828.

Okino, K., Matsuda, K., Christie, D.M., Nogi, Y. & Koizumi, K.-I., 2004. Development of oceanic detachment and asymmetric spreading at the Australian-Antarctic Discordance, *Geochem. Geophys. Geosyst.,* **5**(12), Q12012.

Olive, J.A., Behn, M.D. & Tucholke, B.E., 2010. The structure of oceanic core complexes controlled by the depth distribution of magma emplacement, *Nat. Geosci.,* **3,** 491–495.

Parker, R.L., 1972. The rapid calculation of potential anomalies, *Geophys. J. R. astr. Soc.,* **31,** 447–455.

Parnell-Turner, R., Sohn, R.A., Peirce, C., Reston, T.J., MacLeod, C.J., Searle, R.C. & Simão, N.M., 2017. Oceanic detachment faults generate compression in extension, *Geology,* **45**(10), 923–926.

Peirce, C., 2014a. The role and detachment of faulting at slow-spreading mid-ocean ridges: RRS James Cook cruise report JC102, Durham University (unpublished), pp. 19, https://www.bodc.ac.uk/resources/inventories/cruise_inventory/reports/jc102.pdf.

Peirce, C., 2014b. The role and detachment of faulting at slow-spreading mid-ocean ridges: RRS James Cook cruise report JC109, Durham University (unpublished), pp. 26, https://www.bodc.ac.uk/resources/inventories/cruise_inventory/reports/jc109.pdf.

Peirce, C. & Navin, D.A., 2002. The RAMESSES experiment – V. Crustal accretion at axial volcanic ridge segments – a gravity study at 57°45'N on the slow spreading Reykjanes Ridge, *Geophys. J. Int.,* **149,** 76–94.

Peirce, C., Turner, I.M. & Sinha, M.C., 2001. Crustal structure, accretionary processes and rift propagation: a gravity study of the intermediate-spreading Valu Fa Ridge, Lau Basin, *Geophys. J. Int.,* **146,** 53–73.

Pertsev, A.N., Bortnikov, L.Y., Vlasov, E.A., Beltenev, V.E., Dobretsova, I.G. & Ageeva, O.A. 2012. Recent massive sulphide deposits of the Semenov ore district, Mid-Atlantic Ridge, 1331'N: associated rocks of the oceanic core complex and their hydrothermal alteration, *Geol. Ore Deposits,* **54,** 334–346.

Pertsev, A.N., Bortnikov, N.S., Aranovich, L.Y., Vlasov, E.A., Beltenev, V.E., Ivanov, V.N. & Simakin, S.G., 2009. Peridotite-melt interaction under transitional conditions between the spinel and plagioclase facies beneath the Mid-Atlantic Ridge: insight from peridotites at 13° N, *Petrol.,* **17,** 124–137.

Phipps Morgan, J. & Forsyth, D.W., 1988. Three-dimensional flow and temperature perturbations due to a transform offset:effects on oceanic crustal and mantle structure, *J. geophys. Res.,* **93,** 2995–2966.

Pockalny, R.A., Detrick, R.S. & Fox, P.J., 1988. Morphology and tectonics of the Kane Transform from Sea Beam bathymetry data, *J. geophys. Res.,* **93,** 3179–3193.

Pockalny, R.A., Gente, P. & Buck, R., 1996. Oceanic transverse ridges: a flexural response to fracture-zone-normal extension, *Geology,* **24**(1), 71–74.

Ranero, C.R. & Reston, T.J., 1999. Detachment faulting at ocean core complexes, *Geology,* **27**(11), 983–986, doi:10.1130/0091-7613(1999)027<0983:DFAOCC>2.3.CO;2.

Reston, T. & Peirce, C., 2016. The role and detachment of faulting at slow-spreading mid-ocean ridges: RRS James Cook cruise report JC132, Durham University (unpublished), pp. 62, https://www.bodc.ac.uk/resources/inventories/cruise_inventory/reports/jc132.pdf.

Reston, T.J., 2018. Flipping detachments: The kinematics of ultraslow spreading ridges, *Earth planet. Sci. Lett.,* **503,** 133–157.

Reston, T.J. & Ranero, C.R., 2011. The 3-D geometry of detachment faulting at mid-ocean ridges, *Geochem. Geophys. Geosyst.,* **12,** doi:10.1029/2011GC003666.

Reston, T.J., Weinrebe, W., Grevemeyer, I., Flueh, E.R., Mitchell, N.C., Kirstein, L., Kopp, C. & Kopp, H., 2002. A rifted inside corner massif on the Mid-Atlantic Ridge at 5° S, *Earth planet. Sci. Lett.,* **200,** 255–269.

Roland, E., Lizarralde, D., McGuire, J.J. & Collins, J.A., 2012. Seismic velocity constraints on the material properties that control earthquake behaviour at the Quebrada-Discovery-Gofar transform faults, East Pacific Rise, *J. geophys. Res.,* **117,** B11102.

Sauter, D. *et al.*, 2013. Continuous exhumation of mantle-derived rocks at the Southwest Indian Ridge for 11 million years, *Nat. Geosci.,* **6**(4), 314–320.

Schouten, H., Smith, D.K., Cann, J. & Escartín, J., 2010. Tectonic vs magmatic extension in the presence of core complexes at slow-spreading ridges from a visualisation of faulted seafloor topography, *Geology,* **38,** 615–618.

Searle, R., Murton, B., Mallows, C., Casey, J., Achenbach, K., Unsworth, S. & Harris, M., the JC007 Scientific Party, 2007c. Development of oceanic core complexes on the Mid-Atlantic Ridge at 13–14N: Deep-towed geophysical measurements and detailed seafloor sampling, T51F-01, American Geophysical Union, Fall Meeting, San Francisco.

Searle, R.C., Cannat, M., Fujioka, K., Mével, C., Fujimoto, H., Bralee, A. & Parson, L., 2003. FUJI Done: a large detachment fault near 64° E on the very slow-spreading Southwest Indian Ridge, *Geochem. Geophys. Geosyst.,* **4**(8), 9105, doi:10.1029/2003GC000519.

Searle, R.C. & Laughton, A.S., 1977. Sonar studies of the Mid-Atlantic Ridge crest near Kurchatov fracture zone, *J. geophys. Res.,* **82,** 5313–5328.

Searle, R.C., MacLeod, C., Peirce, C. & Reston, T.J., 2018. The Mid-Atlantic Ridge near 13°20'N: high-resolution magnetic and bathymetric imaging, *Geochem. Geophys. Geosyst.,* doi:10.1029/2018GC007940.

Searle, R.C., MacLeod, C.J. & Murton, B.J. the Shipboard Scientific Party, 2007a. RRS James Cook Cruise JC007: Geological and geophysical studies of the Mid-Atlantic Ridge, 12°30'N to 14°30'N, *Cruise Report,* Durham University (unpublished), pp. 59, https://www.bodc.ac.uk/resources/inventories/cruise_inventory/reports/jc007.pdf.

Searle, R.C., Mallows, C. & Cipcigan, F. the JC007 Scientific Party, 2007b. Mid-Atlantic Ridge at 13–14N: Evidence of unstable seafloor spreading processes from deep-towed magnetic measurements, T53B-1308, American Geophysical Union, Fall Meeting, San Francisco.

Searle, R.C., Tominaga, M., Peirce, C., Reston, T.J. & MacLeod, C.J., 2016. Near-bottom high resolution magnetic observation over and around an active oceanic core complex, MAR 13° N, T33A-2999, American Geophysical Union, Fall Meeting, San Francisco.

Seher, T., Crawford, W.C., Singh, S.C. & Cannat, M., 2010b. Seismic layer 2A variations in the Lucky Strike segment at the Mid-Atlantic Ridge from reflection measurements, *J. geophys. Res.,* **115,** B07107, doi:10.1029/2009JB006783.

Seher, T., Crawford, W.C., Singh, S.C., Cannat, M., Combier, V. & Dusunur, D., 2010c. Crustal velocity structure of the Lucky Strike segment of the Mid-Atlantic Ridge at 37° N from seismic refraction measurements, *J. geophys. Res.,* **115,** Q03011.

Seher, T., Singh, S.C., Crawford, W.C. & Escartín, J., 2010a. Upper crustal velocity structure beneath the central Lucky Strike segment from seismic refraction measurements, *Geochem. Geophys. Geosyst.,* **11,** Q05001.

Severinghaus, J.P. & Macdonald, K.C., 1988. High inside corners at ridge-transform intersections, *Mar. Geophys. Res.,* **9**(4), 353–367.

Simão, N.M., Peirce, C., Falder, M., Reston, T.J., MacLeod, C.J. & Searle, R.C., 2016. Velocity structure of the crust at 13° N on the Mid-Atlantic Ridge: implications for crust accretion and oceanic core complex formation, T33A-2997, American Geophysical Union, Fall Meeting, San Francisco.

Simão, N.M., Peirce, C., Searle, R.C., Reston, T. & MacLeod, C., 2019. Mid-Atlantic Ridge at 13° N: a 3D tomographic view of complex crustal structure and time-varying tectonic and magmatic spreading processes, *Geophys. J. Int.,* forthcoming.

Singh, S.C. *et al.*, 2006. Discovery of a magma chamber and faults beneath a Mid-Atlantic Ridge hydrothermal field, *Nature,* **442,** 1029–1032.

Sinha, M.C. & Louden, K.E., 1983. The Oceanographer Fracture Zone. 1. Crustal structure from seismic refraction studies, *Geophys. J. Royal ast. Soc.,* **75**(3), 713–736.

Smith, D.K., Cann, J.R. & Escartin, J., 2006. Widespread active detachment faulting and core complex formation near 13° N on the Mid-Atlantic Ridge, *Nature,* **443,** 440–444.

Smith, D.K., Escartin, J., Schouten, H. & Cann, J.R., 2008. Fault motion and core complex formation: significant processes in seafloor formation at slow-spreading mid-ocean ridges (Mid-Atlantic Ridge, 13°-15° N), *Geochem. Geophys. Geosyst.,* **9,** Q03003.

Talwani, M., Worzel, J.L. & Landisman, M., 1959. Rapid gravity computations for two-dimensional bodies with application to the Mendocino submarine fracture zone, *J. geophys. Res.,* **64,** 49–59.

Tani, K., Dunkley, D.J. & Ohara, Y., 2015. Termination of backarc spreading: zircon dating of a giant oceanic core complex, *Geology,* **39,** 47–50.

Thébault, E. *et al.*, 2015. International geomagnetic reference field: the 12th generation, *Earth, Planets and Space,* **67,** 67–79, doi:10.1186/s40623-015-0273-4.

Tucholke, B.E., Humphris, S.E. & Dick, H.J.B., 2013. Cemented mounds and hydrothermal sediments on the detachment surface at Kane Megamullion: a new manifestation of hydrothermal venting, *Geochem. Geophys. Geosyst.,* **14,** 3352–3378.

Tucholke, B.E. & Lin, J., 1994. A geological model for the structure of ridge segments in slow spreading ocean crust, *J. geophys. Res.,* **99,** 11 937–11 958.

Tucholke, B.E., Lin, J. & Kleinrock, M., 1998. Megamullions and mullion structure defining oceanic metamorphic core complexes n the Mid-Atlantic Ridge, *J. geophys. Res.,* **103,** 9857–9866.

Tucholke, B.E., Lin, J., Kleinrock, M.C., Tivey, M., Reed, T.B., Goff, J. & Jaroslow, G.E., 1997. Segmentation and crustal structure of the western Mid-Atlantic Ridge flank, 25°25'-27°10'N and 0–29 m.y., *J. geophys. Res.,* **102,** 10 203–10 223.

Tucholke, B.E. & Schouten, H., 1988. Kane fracture zone, *Mar. Geophys. Res.,* **10,** 1–39.

Tuzo Wilson, J., 1965. A new class of faults and their bearing on continental drift, *Nature,* **207,** 343–347.

van Avendonk, H.J.A., Harding, A.J., Orcutt, J.A. & McClain, J.S., 1998. A two-dimensional tomography study of the Clipperton transform fault, *J. geophys. Res.,* **103,** 17 885–17 899.

van Avendonk, H.J.A., Harding, A.J., Orcutt, J.A. & McClain, J.S., 2001. Contrast in crustal structure across the Clipperton transform fault from travel time tomography, *J. geophys. Res.,* **106**(B6), 10 961–10 981.

van Avendonk, H.J.A., Hayman, N.W., Harding, J.L., Grevemeyer, I., Peirce, C. & Dannowski, A., 2017. Seismic structure and segmentation of the axial valley of the Mid-Cayman spreading center, *Geochem. Geophys. Geosyst.,* **18**(6), 2149–2161.

Wessel, P. & Smith, W., 1998. New, improved version of Generic Mapping Tools released, *EOS, Trans. Am. geophys. Un.,* **79,** 579.

White, R.S., Detrick, R.S., Sinha, M.C. & Cormier, M.H., 1984. Anomalous seismic crustal structure of oceanic fracture zones, *Geophys. J. Royal ast. Soc.,* **79**(3), 779–798.

White, R.S., Mckenzie, D. & O'Nions, R.K., 1992. Oceanic crustal thickness from seismic measurements and rare earth element inversions, *J. geophys. Res.,* **97,** 683–715.

Whitmarsh, R.B. & Calvert, A.J., 1986. Crustal structure of Atlantic fracture zones, 1, The Charlie-Gibbs fracture zone, *Geophys. J. Royal ast. Soc.,* **85,** 107–138.

Wilson, S.C., Murton, B.J. & Taylor, R.N., 2013. Mantle composition controls the development of an oceanic core complex, *Geochem. Geophys. Geosyst.,* **14,** 1–18.

Xu, M., Canales, J.P., Tucholke, B.E. & DuBois, D.L., 2009. Heterogeneous seismic velocity structure of the upper lithosphere at Kane oceanic core complex, Mid-Atlantic Ridge, *Geochem. Geophys. Geosyst.,* **10,** Q10001.

Zelt, C.A., 1998. Lateral velocity resolution from three-dimensional seismic refraction data, *Geophys. J. Int.,* **135,** 1101–1112.

Zelt, C.A. & Barton, P.J., 1998. Three-dimensional seismic refraction tomography: a comparison of two methods applied to data from the Faeroe Basin, *J. geophys. Res.,* **103,** 7187–7210.

Zelt, C.A. & Ellis, R.M., 1988. Practical and efficient ray tracing in two dimensional media for rapid traveltime and amplitude forward modelling, *Can. J. Explor. Geophys.,* **21,** 16–31.

Zelt, C.A. & Smith, R.B., 1992. Seismic traveltime inversion for 2-D crustal velocity structure, *Geophys. J. Int.,* **108,** 16–34.

Zhao, M., Canales, J.P. & Sohn, R.A., 2012. Three-dimensional seismic structure of a Mid-Atlantic Ridge segment characterized by active detachment faulting (Trans-Atlantic Geotraverse, 25°55'N-26°20'N), *Geochem. Geophys. Geosyst.,* **13,** Q0AG13.